T.R.
BOLU ABANT İZZET BAYSAL UNIVERSITY
INSTITUTE OF GRADUATE STUDIES
Department of Physics

A STUDY ON DIM-8 NEUTRAL TRIPLE GAUGE COUPLINGS VIA ZZ PRODUCTION AT FUTURE HADRON COLLIDERS

MASTER OF SCIENCE

SAFWA HAITHAM JAMEEL

ACADEMIC SUPERVISOR
Prof. Dr. Haluk DENIZLI
ACADEMIC CO-SUPERVIZOR
Prof. Dr. Abdulkadir SENOL

BOLU, NOVEMBER- 2022

APPROVAL OF THE THESIS

A STUDY ON DIM-8 NEUTRAL TRIPLE GAUGE COUPLINGS VIA ZZ PRODUCTION AT FUTURE HADRON COLLIDERS submitted by **Safwa Haitham JAMEEL** and defended before the Examining Committe Members listed below in partial fulfillment of the requirements for the degree of **Master of Science** in **Department of Physics, Institute of Graduate Studies of Bolu Abant Izzet Baysal University in 16.11.2022** by

Examining Committee Members	**Signature**
Supervisor Prof. Dr. Haluk DENIZLI Bolu Abant Izzet Baysal University	....
Supervisor Prof. Dr. Ilkay TURK CAKIR Ankara University	....
Assoc. Pro Assoc. Prof. Dr. Ali YILMAZ Bolu Abant Izzet Baysal University	....

Prof. Dr. İbrahim KÜRTÜL
Director of Instıtute of Graduate Studies

ETHICAL DECLARATION

In this thesis dissertation that was properly prepared according to the Thesis Writing Rules of Bolu Abant İzzet Baysal University of the Institute of Graduates Studies, I hereby declare that;

- All data, information, and documents presented in the thesis were obtained in accordance with the academic and ethical rules,
- All data, documents, assessments, and results were presented in accordance with the scientific ethical and moral rules,
- All works that were benefitted in the thesis were appropriately cited,
- No alteration was made in the data used,
- Study presented in this thesis is original,

Otherwise, I declare that I accept the loss of all my rights in case any contradiction that may arise against me.

Based on the plagiarism report that was generated on the date of 6/10/2022 by using predetermined filtrations set by Directorate of Institute of Graduate Studies of the Turnitin programme, a plagiarism detection sofware, the similarity index detected was 29 %.

____

Safwa Haitham JAMEEL

ABSTRACT

A STUDY ON DIM-8 NEUTRAL TRIPLE GAUGE COUPLINGS VIA ZZ PRODUCTION AT FUTURE HADRON COLLIDERS
MSC THESIS
SAFWA HAITHAM JAMEEL
BOLU ABANT IZZET BAYSAL UNIVERSITY
INSTITUTE OF GRADUATE STUDIES
DEPARTMENT OF PHYSICS
(SUPERVISOR: PROF. DR. HALUK DENIZLI)
(CO-SUPERVISOR: PROF. DR. ABDULKADIR SENOL)
BOLU, OCTOBER 2022
(Xiii + 66)

Up to date, the Standard Model is in agreement with most of the available experimental data. However, SM does not allow for neutrino masses observed experimentally. Other failures of the SM include the absence of gravity in its formalism and the absence of Dark Matter candidates. All these issues indicate that there is a need for a new physics beyond SM.

The non-abelian feature of the $\mathrm{SU}\,(2)_L$ gauge symmetry, one of the gauge symmetry groups in the SM, prevents self-interactions such as ZZZ and and $ZZ\gamma$ at tree-level. The coupling constants of these interactions are referred as neutral triple gauge couplings (NTGC). These couplings are present in many extensions beyond SM physics. Consequently, the signature of new physics beyond SM can be searched through the possible deviation from the predicted SM values of NTGC.

In this thesis, we investigate the sensitivity of anomalous triple gauge couplings via pp→ZZ process for various future circular hadron colliders options (HL-LHC, HE-LHC, LE-FCC, and FCC) with Effective Field Theory Approach. For these colliders, we find that the limits on all effective couplings derived from the processes under consideration are loose in the case of HL-LHC collider. Besides, we show that the FCC-hh collider gives the best 95% C.L limits on all effective couplings compared to the other colliders. Moreover, our derived limits on all effective couplings are stringint compared to the ones reported by ATLAS and CMS collaborations as will be displayed in the thesis.

KEYWORDS: Triple Gauge Couplings, Beyond Standard Model, Future Circular Colliders, Effective Field Theory.

ÖZET

GELECEK HADRON ÇARPIŞTIRICILARINDA ZZ ÜRETİMİ YOLUYLA DIM-8 YÜKSÜZ ÜÇLÜ AYAR KUPLAJLARI ÜZERİNE BİR ÇALIŞMA
YÜKSEK LİSANS TEZİ
SAFWA HAİTHAM JAMEEL
BOLU ABANT İZZET BAYSAL ÜNİVERSİTESİ
LİSANSÜSTÜ EĞİTİM ENSTİTÜSÜ
FİZİK ANABİLİM DALI

(TEZ DANIŞMANI: PROF. DR. HALUK DENIZLI)
(İKİNCİ DANIŞMAN: PROF. DR. ABDULKADIR SENOL)
BOLU, KASIM- 2022
(Xiii + 66)

Güncel olarak, Standart Model mevcut deneysel verilerin çoğuyla uyumludur. Ancak SM, deneysel olarak gözlemlenen nötrino kütlelerine izin vermez. SM'nin diğer başarısızlıkları, formalizminde yerçekiminin olmaması ve Karanlık Madde adaylarının olmamasını içerir. Tüm bu hususlar, SM'nin ötesinde yeni bir fiziğe ihtiyaç olduğunu göstermektedir.
SM'deki ayar simetri gruplarından biri olan SU $(2)_L$ ayar simetrisinin değişmeyen özelliği, ağaç seviyesinde ZZZ ve ZZγ gibi kendi kendine etkileşimleri engeller. Bu etkileşimlerin eşleşme sabitleri, yüksüz üçlü ayar kuplajları (NTGC) olarak adlandırılır. Bu bağlantılar, SM fiziğinin ötesinde birçok uzantıda mevcuttur. Sonuç olarak, SM'nin ötesindeki yeni fiziğin imzası, NTGC'nin tahmin edilen SM değerlerinden olası sapma yoluyla aranabilir.
Bu tezde, Efektif Alan Teorisi Yaklaşımı ile gelecekteki çeşitli dairesel hadron çarpıştırıcı seçenekleri (HL-LHC, HE-LHC, LE-FCC ve FCC) için $pp \to ZZ$ işlemi aracılığıyla anormal üçlü ayar kaplinlerinin duyarlılığını araştırıyoruz. Bu çarpıştırıcılar için, HL-LHC çarpıştırıcısı durumunda, söz konusu süreçlerden türetilen tüm etkili bağlantıların sınırlarının gevşek olduğunu bulduk. Öte yandan, FCC-hh çarpıştırıcısının diğer çarpıştırıcılara kıyasla tüm etkin kuplajlarda en iyi 95 % C.L limitlerini verdiğini gösteriyoruz. Ayrıca, tüm etkin kuplajlar için elde edilen limit değerleri ATLAS ve CMS iş birlikleri tarafından rapor edilen değerlerden daha iyi olduğu tez çalışmasında gösterilmektedir.

ANAHTAR KELİMELER: üçlü ayar kuplajları, SM Ötesi, Gelecek Dairesel Carpıştırıcıları, Efektif Alan Teorisi

TABLE OF CONTENTS

LIST OF FIGURES

Page

LIST OF TABLES

LIST OF ABBREVIATIONS AND SYMBOLS

ATLAS	: A Toroidal LHC Apparatus.
BSM	**:** Beyond Standard Model.
CERN	: Conseil Europeen Pour Ia reche nucleaire.
c.m.e	: Center of mass energy.
CMS	: Compact Muon Solenoid.
EFT	**:** Effective Field Theory.
FCC-hh	**:** Future Circular Collider
HE-LHC	**:** High Energy Large Hadron Collider.
HL-LHC	: High Lumi Large Hadron Collider.
LE-FCC	**:** Low Energy
LHC	**:** Large Hadron Collider.
$\boldsymbol{L_{int}}$	: integrated luminosity
MC	**:** Monte Carlo.
nTGCs	**:** neutral Triple Gauge Couplings.
NP	: New Physics.
SM	**:** Standard Model.
PDFs	**:** Parton Distribution Functions
TeV	: Tera-Electron Volts.
TGCs	**:** Triple Gauge Couplings
UFO	**:** Universal FeynRules Output

ACKNOWLEDGEMENTS

I would like to express my deep gratitude to Prof. Dr. Haluk Denizli, for his kindness, encouragement, guidance and assistance both as teacher and a supervisor. I deeply thank him for his important contribution to this thesis, particularly from suggesting the problem and stimulating discussion during the course of this work. I appreciate also very much his useful suggestions and corrections.

I would like also to thank Prof. Dr. Abdulkadir Senol for his precious contributions to my knowledge about physics and his support in performing the assigned projects. His guidence also is of highly appreciation. I would like to thank the members of phyics department and the institute of graduate studies at Bolu Abant İzzet Baysal University where this work was carried out.

Finally, I would like to express my deep appreciation to my father, mother, my sister and my beautiful child Aya for their love and support during the course of preparation of the thesis and to whome I dedicate this work.

1. INTRODUCTION

Studying boson pair production in proton-proton (pp) collisions at Hadron Colliders can be useful to investigate the electroweak sector of the SM as well as to search for new physics beyond SM (1-2). The production of two Z bosons, is one of these boson pair production processes, can also be used to search for neutral triple gauge boson couplings which are forbidden in the Standard Model at tree-level.

At the future hadron colliders, two hadrons collide each other to give the possibility for testing the SM at high energies and/or high luminosities and for searching for physics beyond the SM (3-4). One of the possible ways to explore such physics is to analyze data obtained from the collisions aiming to find resonances of new particles for example in mass spectra (4). Another way is to search for couplings between particles that are not allowed in the SM at tree-level. In searching for new physics, it turns to be necessary to have very accurate predictions (4). As it is known, there are many parameters required in the prediction of a given process. Many of these parameters cannot be evaluated theoretically and hence one needs to extract them from data.

In the SM, couplings of three neutral gauge bosons, such as ZZZ, are not allowed at tree-level, but it is possible to search for signatures of such anomalous triple gauge couplings that can arise from new physics beyond SM. For instances, those signatures can be seen as enhancements in tails of distributions that are correlated to the energy of the outgoing leptons in the final states after decaying of the Z bosons (4). This can be the reason why this search strongly profits from an increased center of mass energy which will be the case in future hadron colliders.

The thesis is organized as follows: In chapter 1, we briefly give an introduction to the SM. Then, we make an overview of the electroweak interactions and Triple Gauge Couplings (TGCs). Moreover, we move to Beyond Standard Model (BSM) where we point out some questions not answered by SM and highlight the Effective Field Theory (EFT) approach for neutral triple gauge couplings (nTGCs). In chapter 2, we shed light on the possible future hadron collider projects namely, HL-LHC, HE-LHC, LE-FCC and FCC. The aim and scope of the study in this thesis will be presented in chapter 3. Particularly, we will investigate the sensitivity of anomalous triple gauge couplings via $pp \rightarrow ZZ$ production in the different decay channels of Z boson for various future circular hadron colliders options (HL-LHC, HE-LHC, LE-FCC, and FCC) with Effective Field Theory Approach. We will consider specific decay channels of the produced final state Z bosons where one of the two Z bosons decays to two jets and the other decays to two leptons or to two neutrinos i.e., $qqll$ or $qq\nu\nu$ final states. In addition, we will study the decay channels arising when one of the two Z bosons decays to two leptons and the other decays to two leptons or two neutrinos that is to say the final states $llll$ or $ll\nu\nu$. Chapter 4 is devoted for displaying the methods used in carrying out the required calculations in this study namely, using Madgraph program. Then, we present our results for the cross sections of $pp \rightarrow ZZ$, kinematic distributions of final state particles and sensitivity. Finally, we give our conclusion in chapter 5.

1.1 Standard Model of Particle Physics

The theory describing the fundamental particles and their interactions via the electromagnetic interaction, the weak nuclear interaction (5) and the strong nuclear interaction (6) was given a name known as the standard model in the 1970s (7-8-9). At that time, the SM incorporated all known subatomic particles and predicted the presence of new particles discovered later such as $\boldsymbol{W}^{\pm}$ and Z bosons. Our current understanding is that the SM provides a description of the elementary particles such as leptons, quarks, gauge bosons and the Higgs boson which are shown in figure1.1.

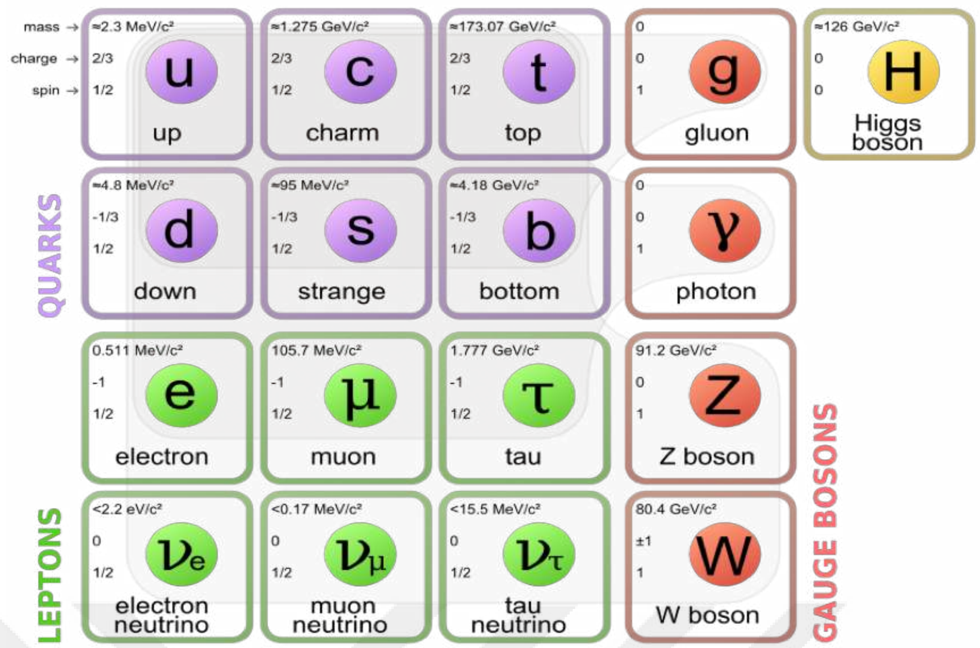

Figure 1.1. particles and bosons content of the standard model (10).

Fermions

The fermionic part of the standard model involves leptons and quarks. A quark is a fermion with half-integer spin. Quarks form hadrons like protons and neutrons, that are constituents of the nucleus of the atom. Quarks and antiquarks are the only particles that interact via the four main interactions : electromagnetism, gravitation, the strong and weak interactions. Quarks have six flavors: up quark, down quark, top quark, bottom quark, charm quark, and strange quark. Quarks with an electric charge equal (+2/3) of the charge of the electron are named as up-type quarks, while quarks with an electric charge of (- 1/3) of the charge of electron are known as down-type quarks.

Leptons have 3 generations of doublets with left-handed chirality and singlets with right-handed chirality.

Gauge bosons

Gauge bosons mediate the basic interactions of natüre (11). They act as the carriers of forces. For inistances, photons are gauge bosons which are the carrier of the electromagnetic interaction. On the other hand, the W^+, W^- and Z bosons are the carriers of the weak interaction while gluons mediate the strong nuclear interaction [26]. All of these gauge bosons are vector bosons and have a spin of 1. Photons and gluons are massless while W^+, W^- and Z bosons have masses.

The Z boson plays an important role in particle physics. As it is known, neutrinos are the most aboundant particles in our Univere. They are electrically and colorly neutral and hence cannot interact through electromaagnetic and strong nuclear forces. They have tiny masses and so there gravitional interactions are almost negligible. Thus, they can only interact with weak nuclear force. Without Z boson, neutrinos cannot interact among themselves using this force. The Z boson was first discovered as mediator of a new type of neutrino reaction the so-called "neutral current interaction". At the end of the 1970s, CERN converted what was then its largest accelerator, known as the Super Proton Synchrotron, to operate as a proton-antiproton collider. The aim of the collider was to produce W and Z bosons directly. Both particles were observed for the first time in 1983 at that collider. The Z boson was then studied in great details at CERN and at Fermi National Accelerator Laboratory in the US. During the 1990s, millions of Z bosons were produced for more studies at the Large Electron-Positron collider at CERN and the SLAC Linear Collider in the US. With the operation of the LHC, more studies related to Z boson were carried out.

The Z boson is very massive particle and has a very short lifetime. Thus, it can travel only a very tiny distance. This explains why, contrary to the common light (made of photons), we don't see a "light" of Z bosons in our everyday-life. However, in extreme conditions of the early Universe and of supernovae explosions, the Z boson is a "daily" particle. The Z boson can be produced at high energies at colliders. Once it is produced and due to its short lifetime, Z boson can decay into a pair of charged leptons (electron-antielectron and muon-antimuon), or a pair of quarks or a pair of neutrinos (neutrino-antineutrino).

Higgs boson

The SM particle content has also Higgs boson which has a spin zero. Moreover, it has no electric and color charge and its interactions with other particles is proportional to their masses. Its lifetime is very short and hence it decays very quickly into other particles.

The SM is a gauge theory stemming from the product of the gauge groups describing the electromagnetic, the weak, and the strong interactions. Each force is described by a gauge group and acts between particles due to the existence of a property of those particles. The electric charge is the property related to the electromagnetic force, the color charge is the property related to the strong force, and the flavor is the propert related to the weak force. The SM has the gauge symmetry structure $\mathrm{SU}(3)_C \times \mathrm{SU}(2)_L \times \mathrm{U}(1)_Y$, where C, L and Y denote the color, left-handed chirality and hypercharge respectively. Each symmetry group is associated with gauge bosons that play the role of the carrier or the mediator of the force.

1.1.1 Electroweak Interactions

At high energies above the electrweak scale, the electromagnetic and the weak interactions begin to look more and more alike and thus are referred as the electroweak interactions. Moreover, above this scale, these two interactions can be described mathematically by one model known as electroweak theory (EWT). This theory is based on the gauge group $\mathrm{SU}(2)_L \times \mathrm{U}(1)_Y$ and thus has four-gauge bosons; B_μ, W_μ^1, W_μ^2 and W_μ^3. Upon breaking the electroweak symmetry via Higgs mechanism W_μ^1 and W_μ^2 are combined to form $W^\pm$ while W_μ^1 and B_μ form both photon and Z boson. Quark, charged leptons, $W^\pm$ and Z bosons acquire their masses tthrough the Higgs mechanisim (12-13-14). Their interactions with each other and with Higgs will follow directly after the electroweak symmetry breaking through the Higgs mechanisim as we will show in the following.

The SM contains a $\mathrm{SU}(2)_L$ doublet scalar field denoted by Φ representing the Higgs field with Y = 1. It can be parameterized as (11)

$$\Phi = \begin{pmatrix} \phi^+ \\ \phi^0 \end{pmatrix} \tag{1.1}$$

where ϕ^+ is electrically charged complex field and ϕ^0 is electrically neutral complex field. This scalar field Φ can be described by the Lagrangian

$$L_{scalar} = (D^{\mu}\Phi)(D_{\mu}\Phi)^{\dagger} - V(\Phi). \quad (1.2)$$

In the above equation, V expresses the potential giving by

$$V(\Phi) = -\mu^2\Phi^{\dagger}\Phi + \lambda(\Phi^{\dagger}\Phi)^2 \,. \quad (1.3)$$

here λ is a positive parameter to ensure that V is bounded from below. It is direct to show that the potential has a minimum that can be written as

$$\langle\Phi\rangle_0 = \langle 0|\Phi|0\rangle = {}^{\upsilon}/_{\sqrt{2}} \quad (1.4)$$

with $\upsilon = \sqrt{-\mu^2/\lambda}$. It should be remarked that υ is the vacuum expectation value which represents the lowest energy state of the scalar potential i.e., the state with the minimum potential energy. As it is known, only the neutral field of the doublet Φ is allowed to acquire a non-vanishing VEV that breaks the $SU(2)_L$ while other symmetries remain unbroken. In other words, after symmetry breaking, we have $SU(2)_L \otimes U(1)_Y \rightarrow U(1)_Q$. Consequently, photon and gluons will remain massles while Z^0 and $W^{\pm}$ gain the masses (11)

$$M_W^2 = \frac{1}{4}g_2^2\upsilon^2 \,,\; M_Z^2 = \frac{1}{4}(g_2^2 + g_2^2)\upsilon^2 \quad (1.5)$$

This is the well-known proposed Higgs mechanism to generate masses of the gauge bosons, $W^{\pm}$ and Z^0. The same mechanisim can be ued to generate the fermion masses. This is direct using the Lagrangian (11)

$$\mathcal{L}_Y = Y_e^{ij}\,\bar{L}_i\Phi\, e_{Rj} + Y_U^{ij}\,\bar{Q}_i\,\tilde{\Phi}\,u_{Rj} + Y_d^{ij}\,\bar{Q}_i\,\tilde{\Phi}\,d_{Rj} + h.c, \quad (1.6)$$

where $\tilde{\Phi} = i\,\tau_2\,\Phi^*$, $Y_{\tilde{\Phi}} = -1$, and Y_{ij} stands for the couplings of the Yukawa interactions. Upon electroweak symmetry breaking discussed before, one can express the Higgs field Φ as,

$$\Phi = \begin{pmatrix} 0 \\ (v+h)/\sqrt{2} \end{pmatrix} \quad (1.7)$$

after substitution in Eq. (1.6), we obtain the following fermion mass matrices

$$M_r^{ij} = \frac{v}{\sqrt{2}} Y_r^{ij}, r = e, u, d. \quad (1.8)$$

The fermion masses will be obtained after diagonalizing the above matrices using the appropriate unitary transformations. Doing so, we get the fermion masses as:

$$\mathrm{m_e} = \frac{v}{\sqrt{2}} \mathrm{Y_e}, \qquad \mathrm{m_u} = \frac{v}{\sqrt{2}} \mathrm{Y_u}, \qquad \mathrm{m_d} = \frac{v}{\sqrt{2}} \mathrm{Y_d}. \quad (1.9)$$

One of the consequences of the Higgs mechanism is the new scalar field h known as higgs boson that can have decays to charged leptons and light quarks.

We turn now to list the electroweak interactions in details. We list them explicity in the following

- **Charged Current Interactions:**

We start with writing the fermion-fermion charged current interactions. They can be described by the following Lagrangian (11)

$$\mathcal{L}^{CC} = \frac{g}{2\sqrt{2}} \bar{u}^i \gamma^\mu (1-\gamma^5) V_{CKM}^{ij} d^j W_\mu^+ + \frac{g}{2\sqrt{2}} \bar{\nu}^i \gamma^\mu (1-\gamma^5) \ell^i W_\mu^+ + h.c. \quad (1.10)$$

The matrix V_{CKM} is the well-known Cabibbo-Kobayashi-Maskawa matrix (15). It describes the quark mixing in the weak charged currents sector and can be parametrized as

$$V_{CKM} = \begin{pmatrix} c_{12}c_{13} & s_{12}c_{13} & s_{12}e^{-10} \\ -s_{12}c_{23} - c_{12}s_{23}s_{13}e^{i\delta} & c_{12}c_{23} - s_{12}s_{23}s_{13}e^{i\delta} & s_{23}c_{13} \\ s_{12}s_{23} - c_{12}s_{23}s_{13}e^{i\delta} & -c_{12}c_{23} - s_{12}c_{23}s_{13}e^{i\delta} & c_{23}c_{13} \end{pmatrix} \quad (1.11)$$

where $c_{ij} = \cos \theta_{ij}$, $s_{ij} = \sin \theta_{ij}$ and δ is the weak CP violating phase. The charged current mediated by $W^{\pm}$ gauge bosons can be represented diagramatically as in Figure 1.2.

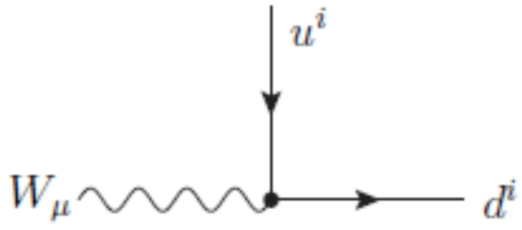

$$-\frac{ig}{\sqrt{2}} V_{CKM}^{ij*} \gamma^\mu P_L$$

Figure 1.2. Feynman diagram of charged current interactions of quarks in the SM.

• Neutral Current Interactions:

Neutral currents in the SM are mediated by the exchanging of Z gauge boson and can be extracted from the Lagrangian

$$\mathcal{L}^{NC} = -\frac{g}{2cos\theta_W} J_\mu^Z Z^\mu \tag{1.12}$$

where $J_\mu^Z = \sum_f q_f \bar{f} \gamma_\mu (g_V^f - g_A^f) f$ with $g_V^f = I_3^f - 2q_f sin^2\theta_W$, $g_A^f = I_3^f$. In figure 1.3 we show the Feynman diagram of Z interactions with fermions in the SM.

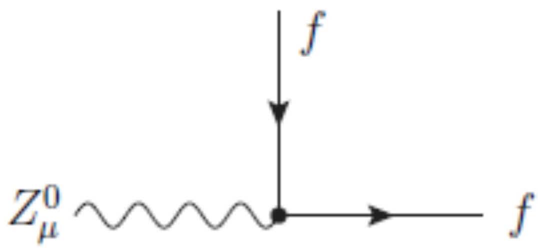

$$-\frac{g}{2cos\theta_W} \gamma^\mu (I_3^f P_L - Q_f cos\theta_W)$$

Figure 1.3. Feynman diagram of Z fermion interactions in the SM.

• Electromagnetic Interactions:

The electromagnetic interactions are those interactions which are mediated by exchanging photons. They only involve electrically charged fermions and can be extracted from the below Lagrangian

$$\mathcal{L}^{EM} = -eJ_{\mu}^{EM}A^{\mu},\ J_{\mu} = -\bar{e}\gamma_{\mu}e + \frac{2}{3}\bar{u}\gamma_{\mu}u - \frac{1}{3}\bar{d}\gamma_{\mu}d. \quad (1.13)$$

They are displayed in Figure 1.4 below.

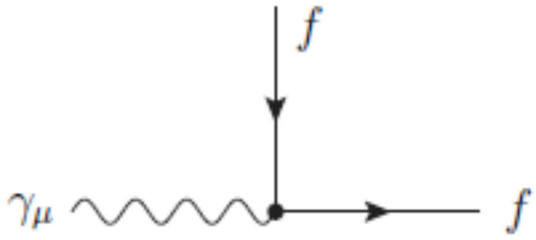

$-i\, eQ_f\, \gamma^{\mu}$

Figure 1.4. Feynman diagram of electromagnetic interactions in the SM where Q_f is the electric charge of the fermion.

The SM Lagrangian can be expressed as (16)

$$\mathcal{L}_{SM} = -\frac{1}{4}G_{\mu\upsilon}^{a}G_{a}^{\mu\upsilon} - \frac{1}{4}F_{\mu\upsilon}^{a}F_{a}^{\mu\upsilon} - \frac{1}{4}B_{\mu\nu}B^{\mu\nu} + L_{i}iD_{\mu}\gamma^{\mu}L_{i} + \bar{e}_{R_i}iD_{\mu}\gamma^{\mu}e_{R_i}$$

$$+\bar{Q}_{i}iD_{\mu}\gamma^{\mu}Q_{i} + \bar{u}_{R_i}iD_{\mu}\gamma^{\mu}u_{R_i} + \bar{d}_{R_i}iD_{\mu}\gamma^{\mu}d_{R_i} \quad (1.14)$$

Where we have three generations or families of quarks and leptons listed below.

$$Q_1 = \binom{u}{d}_L, u_{R_1} = u_R,\ d_{R_1} = d_R, \quad (1.15)$$

$$Q_2 = \binom{c}{s}_L, u_{R_2} = c_R,\ d_{R_2} = s_R, \quad (1.16)$$

$$Q_3 = \binom{t}{b}_L, u_{R_3} = t_R,\ d_{R_3} = b_R, \quad (1.17)$$

$$L_1 = \binom{\nu_e}{e^-}_L, e_{R_1} = e_R, \quad (1.18)$$

$$L_2 = \binom{\nu_\mu}{\mu^-}_L, e_{R_2} = \mu_R, \quad (1.19)$$

$$L_3 = \binom{\nu_\tau}{\tau^-}_L, e_{R_3} = \tau_R, \quad (1.20)$$

With:

$$D_\mu Q_i = \left(\partial_\mu - i g_s T_a G_\mu^a - i g_2 \frac{\tau_a}{2} W_\mu^a - i g_1 \frac{Y_{Qi}}{2} B_\mu\right) Q_i \tag{1.21}$$

$$D_\mu L_i = \left(\partial_\mu - i g_2 \frac{\tau_a}{2} W_\mu^a - i g_1 \frac{Y_{L_i}}{2} B_\mu\right) L_i \tag{1.22}$$

$$D_\mu f_R = \left(\partial_\mu - i g_1 \frac{Y_{f_R}}{2} B_\mu\right) f_R \tag{1.23}$$

With T_a, τ_a and Y denoting the generators of the corresponding gauge symmetry group and g's represent the gauge couplings. The third component of the isospin, I_3, and the electric charge, Q, are related via $Q = I_3 + \frac{Y}{2}$. The field strength tensors appear in Eq. (1.14) are given as:

$$G_{\mu\nu}^a = \partial_\mu G_\nu^a - \partial_\nu G_\mu^a - g_s f^{abc} G_\mu^b G_\nu^c, \tag{1.24}$$

$$W_{\mu\nu}^a = \partial_\mu W_\nu^a - \partial_\nu W_\mu^a - g\epsilon^{abc} W_\mu^b W_\nu^c, \tag{1.25}$$

$$B_{\mu\nu} = \partial_\mu B_\nu - \partial_\nu B_\mu. \tag{1.26}$$

It is clear from the definitions of the field strength tensors $G_{\mu\nu}^a$ and $W_{\mu\nu}^a$ that the gauge bosons of the corresponding groups $SU(3)_C$ and $SU(2)_L$ interact with themselves resulting in triple and quadruple gauge bosons interactions and consequently couplings.

1.1.2 Triple Gauge Couplings (TGCs)

The Triple Gauge Couplings are very interesting features of the SM. The $\boldsymbol{SU(2)_L}$ gauge symmetry, which is one of the gauge symmetry groups in the SM, is non-abelian. This feature of the $\boldsymbol{SU(2)_L}$ gauge symmetry results in the gauge boson self-interactions through the term $\boldsymbol{g_2 \in_{ij\kappa} W_\mu^j W_\nu^\kappa}$ present in the standard model Lagrangian. This term allows self-interactions only between the gauge bosons associated with the $\boldsymbol{SU(2)_L}$ gauge symmetry. However, not all these self-interactions exist. This is depending on the values of the Levi-Civita tensor, $\boldsymbol{\epsilon_{ijk}}$ which takes values either zero or one. In the case that the bosons are the same, the Levi-Civita tensor takes value equals to zero. Thus, in the standard model, at tree level, there are only the self-interaction of the charged $\boldsymbol{W}^{\pm}$ gauge bosons giving rise to the two vertices $\boldsymbol{W^+W^-Z}$ and $\boldsymbol{W^+W^-\gamma}$. On the other hand, as a result of the vanishing of the Levi-Civita tensor, neutral triple gauge boson vertices are absent in the standard model at tree-level. For instances, there are no ZZZ and $ZZ\boldsymbol{\gamma}$ vertecies at tree-level.

In some extensions of new physics beyond the SM neutral triple gauge boson couplings can exist at tree-level. As a result, if the neutral triple gauge couplings are observed in collider, they will indirectly be an evidence of the existence of new physics beyond the standard model. In principle, it is possible that signals from new physics will be seen in this coupling via the discovery of the trilinear Z boson vertex. In fact, lot of questions regarding this possibility need answers. These questions can be summarized as follows; in different extensions of beyond SM physics what do we expect about the sizes of such anomalous effects? or can the New Physics, that yields the anomalous gauge boson couplings, reveals itself in the energy frontier which we are about to reach in current and future colliders?

1.2 Beyond Standard Model (BSM)

The success of the SM in predicting particles and explaining many phenomena with great precision make it a remarkable theory. However, there are number of questions releated to many theoretical and phenomenological issues that cannot be explained within the framework of the SM. In the following we briefly mention the most relevant ones.

1.2.1 Questions not Answered by SM

The most important experimental issues can be summarized as follows: Firstly, astrophysics and cosmological issues such as those related to dark energy and dark matter (17) and cannot be explained by the standard model. Secondly, baryon-antibaryon asymmetry of the universe which is a result of the presence of more matter than anti-matter in our universe (18). In addition, gravity is not included in the standard model. Also, why do we have 19 free parameters and couplings with problems like renormalization? Among the other problems of the standard model is the scale difference encountered in particle physics that is known as the Hierarchy problem. For example, a notable scale differences exists between the Higgs and the Plank mass scales. Finally, in the standard model, quarks and charged leptons acquire masses through Higgs mechanism while neutrinos remain massless. However, it has been proven experimentally that neutrinos have masses.

The inability of the SM to solve the problems mentioned before indicates the necessity of the presence of extensions of the SM. This beyond SM physics can be formulated by enlarging some symmetries or sectors in the SM as follows:

1- Extending the gauge symmetry by adding new gauge groups (19).
2- Extending the Higgs Sector by adding new singlet scalars, new doublets and so on (20).
3- Extending the matter content by adding new fermions, new gauge bosons etc... (21).
4- Extending the space-time dimensions by adding new dimensions such as in Extra-dimensions and string theory (22).
5- Extending the Lorentz Symmetry as in Supersymmetry (23).
6- Incorporating the Gravity as was done in Supergravity (24).

1.2.2 Effective Field Theory (EFT) approach for Neutral Triple Gauge Couplings (nTGCs)

The signature of new physics beyond standard model can be searched, for instances, through the possible deviation from the standard model predictions of the neutral triple gauge (NTG) couplings of the ZZZ and $ZZ\gamma$ vertices. New couplings can contribute to the NTG. They may arise from new phyiscs and can lead to an enhancement of the standard model cross sections. A thorough method to investigate these new couplings is to perform a precision measurement of the Triple Gauge Couplings. In figure 1.5, we show examples of Feynman diagrams of such couplings.

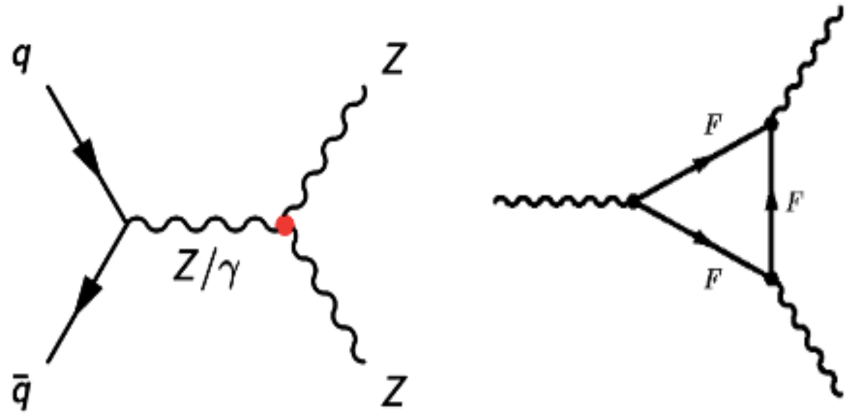

Figure 1.5. Left: Feynman diagram for $q\bar{q} \rightarrow ZZ$ production via the s-channel. Right: triangular fermion loop.

In the literature there are two approaches to study these couplings, namely the anomalous coupling approach (25-26-27-28) and the Effective Field Theory (EFT) approach (29-30-31). From the theoretical point of view, the first approach is not ideal as it is not gauge invariant and leads to violation of unitarity constraints at the LHC energies. On the other hand, the EFT approach is a more powerful model-independent approach which is formulated through adding gauge-invariant higher-dimensional operators to the SM Lagrangian while satisfying the following (32):

• The SM is the most general theory of lepton and quark fields, along with a single scalar Higgs doublet field, respecting the $SU(3)_C \times SU(2)_L \times U(1)_Y$ gauge symmetry. Additionally, all operators constructed from these fields that exist in the SM Lagrangian must have mass dimension restricted to be of four or less.

• Upon adding new higher-dimensional operators, the symmetries of the SM should be respected. These symmetries are the Lorentz invariance and the $SU(3)_C \times SU(2)_L \times U(1)_Y$ gauge symmetry.

• Considering the mass dimensional analysis, the new operators have coefficients of inverse powers of mass. Consequently, they will be suppressed if the mass scale is large in comparison with the experimentally accessible energies.

• The SM must be recovered upon setting an appropriate mass scale limit.

• The theory obtained by any extension of the SM should be general enough to reveal any effects of physics beyond the SM. It should also provide some guidance to the most likely places to explore the signatures of the new physics.

• In theory of beyond SM physics, it should be possible to evaluate the radiative corrections at any order in the SM interactions.

In the EFT approach, the effective Lagrangian, L_{eff}, of the new physics beyond the SM can be generally parametrized as (33)

$$L_{eff} = L_{SM} + \sum_{d>4} \sum_i \frac{C_i}{\Lambda^{d-4}} O_i^d \tag{1.27}$$

Here Λ is the mass scale of the new physics, C_i are the effective coupling strengths and O_i are the possible operators which can be constructed from the SM fields. The SM Lagrangian, L_{SM}, has mass dimension four, and hence the higher order operators must have coecients of inverse mass powers Λ^{d-4} to respect mass dimensionality. The new physics is assumed to exist at a mass scale Λ. This mass scale is much larger than the available energy, $\Lambda >> \hat{s}$. Thus, only first operators in the expansion of equation (1.27) are expected to contribute to the process under concern. The next order operators will be highly suppressed by higher powers of the large mass scale Λ and thus their contributions will be tiny and can be safely dropped.

The lowest odd dimension operators are those of mass dimension 5 and 7. They violate lepton and/or baryon numbers. On the other hand, no dimension six operator contributes to the neutral TGCs. Therfore, the lowest dimension operators that can describe the neutral triple gauge couplings are those with dimension eight. In fact, there are only four dimension eight operators that are respecting the imposed symmetries and generate the neutral TGCs.

Considering both U(1)_EM and Lorentz symmetries, the effective Lagrangian constructed from these four dimension-eight operators can be written as (33)

$$L^{nTGC} = L_{SM} + \sum_i \frac{C_i}{\Lambda^4} (O_i + O_i^{+}). \tag{1.28}$$

Where the operators O_i are given as

$$O_{BW} = \mathrm{i}\, H^{\dagger} B_{\mu\nu} W^{\mu\rho} \{D_{\rho}, D^{\nu}\}\, \mathrm{H}, \tag{1.29}$$

$$O_{WW} = \mathrm{i}\, H^{\dagger} W_{\mu\nu} W^{\mu\rho} \{D_{\rho}, D^{\nu}\}\, \mathrm{H}, \tag{1.30}$$

$$O_{BB} = \mathrm{i}\, H^{\dagger} B_{\mu\nu} B^{\mu\rho} \{D_{\rho}, D^{\nu}\}\, \mathrm{H}, \tag{1.31}$$

$$O_{\tilde{B}W} = \mathrm{i}\, H^{\dagger} \tilde{B}_{\mu\nu} W^{\mu\rho} \{D_{\rho}, D^{\nu}\}\, \mathrm{H}, \tag{1.32}$$

With $\tilde{B}_{\mu\nu}$ and $W_{\mu\nu}$ are the dual strength tensors defined before in Eqs. (1.26) and (1.25) respectively. It turns out that, when the energy scale of new physics is high, main contribution of new physics to the amplitude of the scattering process ff → ZZ is coming from the interference between the SM and the dim-8 operators.

The ATLAS group at the Large Hadron Collider reported the results of the measurement of ZZ production carried out in the final states with two charged leptons and two neutrinos. These results were obtained based on the data collected from the LHC Run-1 and Run-2 in 2015 and 2016 in pp collisions at $\sqrt{s}$ = 13 TeV and corresponding to an integrated luminosity of 36.1 fb^{-1} (36). The reported result indicates no significant deviations from the SM predictions were observed, and hence a strong bound at 95% CL reads [-4.0, 4.0] in units of TeV^{-4} was set on the effective coupling $C_{\tilde{B}W}/\Lambda^4$ (34). It should be remarked that, the analysis was carried out in the $\ell\ell$νν channel with ℓ = e or μ final states, that have larger branching ratios and suffering from higher background contamination compared to the 4 ℓ channel.

The possible bounds on the (aNTGC) contributing to the pp → ZZ production and followed by the process ZZ → $\ell\ell$ νν final state at a 100 TeV future FCC-hh collider have been derived in Ref. (35). In the study, one of the two Z boson was considered to decay into a pair of light charged leptons having the same-flavor but with opposite-sign (muons or electrons) while the second Z boson was taken to decay into two neutrinos. The obtained limits on the charge-parity (CP)-conserving effective couplings $C_{\tilde{B}W}/\Lambda^4$ and CP-violating effective couplings C_{WW}/Λ^4, C_{BW}/Λ^4 and C_{BB}/Λ^4 are evaluated at 95% Confidence Level (C.L.) utilizing the transverse momentum of the dilepton system ($p_{\mathrm{T}}^{\ell\ell}$) are given as [− 0.042, + 0.042],

[− 0.050, + 0.050], [− 0.050, + 0.050], and [− 0.048, + 0.048] in units of TeV^{-4}, respectively.

2. FUTUERE HADRON COLLIDER PROJECTS UNDER CONSIDERATION

The Large Hadron Collider is considered, up to now, the world's highest energy collider with the reached center of mass energy $\sqrt{s}$ = 13 TeV at RUN2 and high luminosity up to $10^{34}\ cm^{-2}\ s^{-2}$ (36-37). It is a hadron-hadron collider that is constructed at CERN, the European Organization for Nuclear Research, in Geneva (Switzerland). With these high center of mass energies and high luminosities, searches at LHC aims to probe new physics or do precise measurements of SM processes in phase spaces that could not be investigated before.

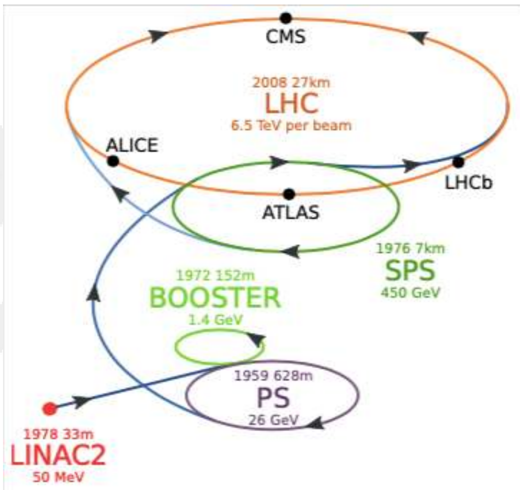

Figure 2.1. Schematic view of the LHC acceleration complex. The maximum beam energy is shown together with the year of the initial startup and the circumference of the individual accelerator. The figure is taken from (38).

At LHC, the Higgs boson was discovered in 2012 (39) which finally gave an answer to one of the outstanding big questions in particle physics of how massive particles in the SM acquire their masses. These particles include quarks, charged leptons, $W^{\pm}$ and Z gauge bosons (12-13-14). Although the great success of the LHC to discover the Higgs boson still some physics program requires next-energy frontier colliders with much higher luminosities and center of mass energies to search for new particles proposed in many extensions of the SM.

One way to advance in the exploration of new physics is to study the Higgs boson, in these new colliders, and see what we can learn from it. To carry out such exploration within unexplored territories, a leap needs to be taken in relation to detector developments. Several future lepton and hadron colliders were been discussed in the literature to highlight the possibilities of extending the energy and luminosity reach much beyond the current LHC (40-41). The high energy physics community in Europe proposed four future hadron collider projects after the Large Hadron Collider (LHC) era; the High-Luminosity Large Hadron Collider (HL-LHC) project, the High-Energy Large Hadron Collider (HE-LHC) project, the Low-Energy FCC (LE-FCC) project and the Future Circular Collider hadron collider (FCC-hh) project. In the upcoming sections of this chapter, we briefly discuss a set of these colliders relevant to our study (42-43).

2.1 The High-Luminosity Large Hadron Collider (HL-LHC) project

The High-Luminosity LHC (HL-LHC) will be a proton-proton future collider. It will be an upgrade of the LHC, aiming to reach an instantaneous luminosity a factor of five larger than the LHC nominal value and to increase the integrated luminosity by a factor of 10 beyond the LHC's targeted value (44-45). Consequently, it will enable the experiments to extend their data sample by one order of magnitude in comparison with the corresponding LHC one. Hence, this will allow physicists to explore known mechanisms in greater detail. One of such mechanisms is the Higgs mechanism. The HL-LHC will produce each year at least 15 million Higgs bosons which should be compared to around three million from the LHC in 2017 (45). Clearly, this extends to a large content the potential to study the characterstics of the Higgs boson and also the mass reach in the search for new particles.

With the running of the HL-LHC, ATLAS and CMS experiments plan to continue the direct search for new particles proposed by many extensions of the SM which is expected to shed light on one or more of the open questions in high energy physics and cosmology such as nature of dark matter. Moreover, the HL-LHC can provide the discovery potential via the precision studies of the flavour sector in rare decays and CP violation in charm and beauty hadrons (46).

The HL-LHC is designed to reuse the present LHC tunnel but with an increase of the center-of- mass collision energy from 13 TeV to an initial value of 14 TeV and with a significant improvement in increasing the luminosity by a factor of five to seven (47).

2.2 The High-Energy Large Hadron Collider (HE-LHC) project

One of the proposed future hadron colliders is the so called the High-Energy LHC (HE-LHC). It is an upgrade of the LHC with pp collisions at about twice the collision energy of the LHC and a total integrated luminosity of 15 ab^{-1}, to be collected during 20 years of its operation. It is planned to utilize the infrastructures present in the tunnel of the LHC, without any increase of the cross section of the tunnel (48-49).

The HE-LHC is planned to extend the HL-LHC reach in direct searches for new particles, nearly doubling the reach in mass of new particles with respect to HL-LHC. Moreover, the HE-LHC will improve the precision of the HL-LHC measurements, particularly in the EW and flavour sectors and exploring in more detail the properties of possible future LHC discoveries. Among the other potentials of the HE-LHC one can mention that new gauge bosons such as a Z', whose reach at the HL-LHC is evaluated to be around 6 TeV, could be observed by the HE-LHC up to a higher mass of $\sim$12 TeV (50). One can also refer to other potentials where the HE-LHC would increase the statistics of the signals and make it possible to analyse their properties in more detail. Besides, it will provide evidence of unconfirmed deviations from the SM.

2.3 The Low-Energy Future Circular Collider (LE-FCC) project

The Low-Energy FCC (LE-FCC) collider is one of the potential intermediate energy proton-proton collider at $\sqrt{s}$ = 37.5 TeV, and an expected integrated luminosity of 10 ab^{-1} during the 20-year running of the project (51). It will use a new 100 km tunnel and dipoles with a magnetic field strength of 6 T, which is remarkably lower than the field strength of 8.7 T in the present LHC.

The physics program planned to be investigated in the LE-FCC includes several searches. For instances, search for weakly interacting massive particles playing the role of dark matter, search for high masses, the signatures for a strong first order electroweak phase transition, and the Higgs precision measurements.

Other searches are listed in Table 2.1 where the 5σ discovery reach is shown for various resonances (52): excited quarks Q∗, Randall-Sundrum gravitons GRS, Z' bosons in the sequential SM and in top-colour (TC) models.

Table 2.1. 5σ discovery reach for various resonances (52): excited quarks Q∗, Randall-Sundrum gravitons GRS, Z' bosons in the sequential SM and in top-colour (TC) models. The rows labeled by CR are obtained by scaling the reach using the Collider Reach PDF extrapolation (51).

collider	$Z'_{SSM} \to \tau^+\tau^-$	$Z'_{SSM} \to t\bar{t}$	$G_{RS} \to WW$	$Z'_{TC} \to t\bar{t}$	$Q^* \to jj$	$Z'_{SSM} \to \ell^+\ell^-$
LE-FCC CR	7.5	7.5	9	10	16	17
LE-FCC	1.25	1.25	1.3	1.25	1.3	1.3

2.4 The Future Circular Collider (FCC) project

The FCC is one of the proposed post-LHC high-energy frontier colliders at CERN. As it is well known, circular hadron colliders are discovery machines where their discovery reach is dependent on the beam energy. With this in mind, an increase in the accelerator circumference to the value 100 km will result in a center of mass energy equals to 100 TeV with similar dipole of a magnetic field 16 T (53). The FCC has two stages. In the first one, it will work as an electron-positron collider (FCC-ee). This collider is referred to as Higgs-factory as it will have the ability to create Higgs bosons on the order of $\mathbf{10^6}$ Higgses. In the second one, the FCC will be upgraded to become a hadron collider, which is known as FCC-hh, where the energy will be a factor 8 of the present energy reach of the LHC i.e., the center of mass energy will be about 100 TeV (54-55-56).

The FCC-hh is a proton–proton collider aiming to obtain an instantaneous luminosity of 30 × 10^{34} cm^{-2} s^{-2} per interaction point and to reach to a total luminosity of 20-30 ab^{-1} after 25 years of operation (54-55). With the extraordinary center of mass collision energy, the FCC-hh will be a unique collider to explore new physics beyond the SM.

The FCC-hh will allow an extensive exploration of new particles predicted by many extensions of the SM that can be searched for directly, owing to the vast mass reach of 100 TeV center of mass energy. In addition, the rate of Higgs pair production events would increase by a factor of 40 at FCC-hh, with respect to its rate at 14 TeV (53). As a consequence, it will enable Higgs self-couplings to be measured with an accuracy reaching 5% (53). The measurement of the Higgs self-couplings with high accuracy would allow, to a large content, to investigate models that rely on modifying the Higgs potential.

In Table 2.2 we show some of the relevant key parameters of FCC-hh, HE-LHC, HL-LHC and LHC, for operation with proton beams for the sake of comparison (49). It is clear from Table 2.2 that, the set of the given colliders FCC-hh, HE-LHC, HL-LHC differ in their center of mass enrgies where the FCC-hh has the highest enrgy. In addition, it has the largest circumference among all other colliders and largest number of bunches/ beams.

Table 2.2. Key parameters of FCC-hh, HE-LHC, HL-LHC, for operation with proton beams. It should be noted that, all values, except for the injection energy, refer to collision energy. The bunch spacing is 25 ns for all colliders (49).

Parameter	unit	FCC-hh	HE-LHC	HL-LHC
centre-of-mass energy	TeV	100	27	14
injection energy	TeV	3.3	0.45/1.3	0.45
arc dipole field	T	16	16	8.33
circumference	km	97.8	26.7	26.7
beam current	A	0.5	1.12	(1.12) 0.58
bunch population Nb	1011	1.0	2.2	(2.2) 1.15
Number ofbunches /beams nb	—	10600	2808	(2760) 2808
Longitudinal emittance (~4πσz σE)	eVs	5	4.2	2.5
norm. transv. rms emittance γε	μm	2.2	2.5	(2.5) 3.75
initial rms IP beam size σx*, y	μm	6.7 3.5	6.6	(8.2) 16.7
peak luminosity per IP	$10^{34}cm^{-2}s^{-1}$	5 30	28	(5, leveled) 1
peak no. of events / crossing	—	170 1000	800	(135) 27
luminosity per year (160 days)	fb^{-1}	≥ 250 ≥ 1000	730	(350) 55

3. AIM AND SCOPE

The aim of this thesis is to investigate the sensitivity of the anomalous triple gauge couplings via $pp \rightarrow ZZ$ production in Effective Field Theory Approach for various future circular hadron colliders under consideration; HL-LHC, HE-LHC, LE-FCC, and FCC-hh. In particular, we aim to study specific decay channels of the produced Z bosons where one of the two Z bosons decays to two jets and the other decays into two leptons or to two neutrinos ($qqll$ or $qq\nu\nu$) as well as one of the two Z bosons decays to two leptons and the other decays into two leptons or two neutrinos ($llll$ or $ll\nu\nu$). The sensitivities of the charge-parity (CP)-conserving $C_{\tilde{B}W}/\Lambda^4$ and CP-violating C_{WW}/Λ^4, C_{BW}/Λ^4 and C_{BB}/Λ^4 couplings are obtained at 95% Confidence Level (C.L.) including the realistic detector effects.

Although the production of two on-shell Z bosons has the smallest cross-section compared with the cross sections of all the diboson processes, it is quite competitive for searches and measurements. The ZZ pair production process is a leading channel in studying the off-shell production of the Higgs particle (57-58) and hence it can probe the electroweak sector of the SM. Moreover, the ZZ pair production permits a direct measurement of the gauge bosons self-couplings. Thus, this production is so important in searching for anomalous neutral triple-gauge-boson couplings (59). In Figure 3.1 and Figure 3.2 we show Feynman diagrams of ZZ production.

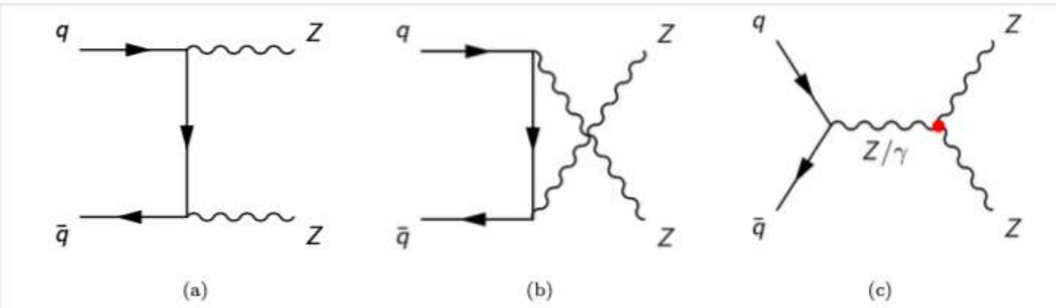

Figure 3.1. Feynman diagrams contributing, at the leading order, to ZZ production via $q\bar{q}$ at hadron colliders. The ZZZ and ZZϒ neutral trilinear vertices which do not exist in the SM at tree level are generated through the s-channel diagram in (c) (60).

Figure 3.2. Gluon fusion producing ZZ dibosons at the hadron colliders (60).

The branching ratios of the Z boson decaying into different channels are well known and are given as 69.9% for qq decay channel, 20.0% for νν decay channel and 10.1% for $\ell^+\ell^-$ decay channel (5). As each Z boson decays independently, the branching ratio for a specific ZZ final state can be evaluated as the product of the branching ratios for the decaying of the two-gauge Z bosons. The branching ratios for the several ZZ decay modes are presented in Table 3.1 (60).

Table 3.1. Branching ratios of different ZZ decay channels (61).

Decay mode	Branching fraction
ZZ→$\ell\ell\ \ell'\ell'$	0.45%
ZZ→$\ell\ell\ \mathcal{VV}$	1.34%
ZZ→$jj\ jj$	48%
ZZ→$\ell\ell\ jj$	9.4%
ZZ→$\mathcal{VV}\ \mathcal{VV}$	4%
ZZ→$\mathcal{VV}\ jj$	36.8%

As can be seen from Table 3.1 the branching fraction of the pair of Z boson decaying into two neutrinos and two charged leptons is so small. However, this four-lepton final state is an important channel to study the anomalous triple gauge couplings. This can be explained as this channel has little background contamination to the signal making it very clean for search for new physics signatures.

4. MATERIAL AND METHODS

Our goal is to find the sensitivity of the anomalous triple gauge couplings via $pp \rightarrow ZZ$ production in the Effective Field Theory Approach for various future circular colliders proposed by high energy physics community. One of the most common tools to start generating events, based on the theory under concern, is MadGraph (62-63-64). The events are generated in Mad Graph by importing the signal implemented through UFO (66) model file into MadGraph5_aMC@NLO v2.6.4 (65). Then, they pass through Pythia for hadronization and showering. On the other hand, LHAPDF v6.1.6 (67) library and its NNPDF v2.3 (68) set is used as the default set of parton distribution functions (PDFs) for all simulated MC samples. Finally, realistic detector effects are added by DELPHES (69). It should be noted that, all events are analyzed by using the ExRootAnalysis (70) package with ROOT v6.16 (71). In this section, detailed discussion of the material and method used in this thesis as well as analysis will be described in the following sections.

4.1 Madgraph

MadGraph is an open-source software written in Python programming language. For any Lagrangian based model (either renormalizable or effective one) implemented in FeynRules via the UFO interface, MadGraph automatically generates matrix elements for the given process at the tree-level and one-loop level (including diagram plotting) and the corresponding helicity amplitude subroutines via the ALOHA package (72). Another powerful feature of MadGraph is its ability to perform complete event simulation at LO (via CKKW and MLM methods) and at NLO (via MC@NLO and Powheg) or the combination of the two ("CKKW at NLO"), which is done through merging to showering/hadronization codes (PYTHIA) (73). Consequently, it can add realistic detector effects with a detector card designed to study specific collider. All these capabilities, offered by MadGraph, are very useful for studying SM and BSM phenomenology.

The Methodology of performing computation using MadGraph program can be summarized as follows: firstly, the user specifies a process with well-defined initial and final state particles. This process should be subjected to a number of refined criteria. These can be, for instances, forced or forbidden s-channel resonances, excluded internal particles, and forced decay chains of final state particles. Secondly, multiparticle labels can be utilized to determine all possible processes involving a range of particles. As a consequence, MadGraph first generates all Feynman diagrams for the process where the objective here is to define the corresponding helicity amplitudes, in accordance with the rules specified by the model. Then, it creates a computer code required to calculate the matrix element at a given phase space point. The evaluation of the matrix element in MadGraph can be achieved using calls to helicity wavefunctions and amplitudes, which were firstly accomplished in the HELAS package (74).

Turning now to the calculations of the cross sections and decay widths, MadGraph produces computer codes which evaluate the cross section or the decay width in addition to event generation, using the MadEvent package (75-65). Basically, the computation of a cross section using MadGraph includes three steps: generation, output, and running. All these steps are carried out by executing on-line commands in the MadGraph shell, that can be accessed by executing from a terminal shell in the main directory. These commands are listed below together with their descriptions.

/bin/mg5 aMC: the prompt now reads: MG5 aMC> which indicates that one is inside the MadGraph5 shell. The three steps stated before are in accordance with the following commands: MG5 aMC> generate the required process MG5aMC> output MG5aMC> launch respectively. When the desired process is generated, the relvant parameters for the run will be stored in various cards (inside the Cards dir): param_card: this card contains all model parameters such as masses, couplings, ...

run_card: in this card one can find all parameters relevant to the collider and run settings including energy, Nevents, cuts, scales, ... pythia_card (MadEvent) / shower_card (aMC): parameters that are required to shower the partonic events

plot_card (MadEvent): which variables to plot delphes/pgs_card: this is for detector simulation

We proceed now to the generation phase where MadGraph5 builds the cross section relevant to the process written as input by the user, for example in our thesis the process is $pp \rightarrow ZZ$. This caan be done by executing the following command:

MG5aMC> generate $pp \rightarrow ZZ$

Giving the process, MadGraph5 carries out the operations mentioned above in methodology of computation. Once the process is generated, the relevant information will be still in the computer memory. In order to proceed, there will be a need for this information to be written on disk. It should be remarked that, when generating a given process, MadGraph presumes that the considered model in the calculations is the SM with b quarks taken to be massive. However, a different model can be considered, by “importing” it before the generation. Currently, in the MadGraph5 library, there are several models that are available for the calculations. These models are built using FeynRules (76-77) and expressed in the Universal FeynRules Output (UFO) format (66). The running phase of MadGraph5 permits to accomplish a diversity of tasks. The most important ones, among these tasks, are the production of unweighted events, and the plotting of user-defined physical observables.

As stated before, the objective of this thesis, is to investigate the sensitivity of the anomalous triple gauge couplings via $pp \rightarrow ZZ$ production in different decay channels of Z boson for various future circular hadron colliders (HL-LHC, HE-LHC, LE-FCC, and FCC) with Effective Field Theory Approach. We will consider the final state channels orginating from the decaying of one of the produced two Z bosons into two neutrinos while the other Z decays to two leptons in addition to another final state channels arising from the decaying of one of the two Z bosons into two neutrinos while the other Z boson decays to two jets. To do this, the expression of the operators listed in Eqs. (1.29 - 1.32) are implemented through FeynRules package (76-77) as a Universal FeynRules Output (UFO) (66). Then, the cross sections of the resultant processes $pp \rightarrow ZZ \rightarrow \ell\ell\nu\nu$ and $pp \rightarrow ZZ \rightarrow qq\nu\nu$ in various future circular hadron colliders at different center of mass energies are calculated with MadGraph5_aMC@NLO (65). Example of shell script (ntgc_cs_pp2zz_cBBL4_FCC.sh) used in MadGraph to scan C_{BB}/Λ^4 coupling between -5 and +5 TeV^{-4} for FCC collider is given in Figure 4.1. The name of the model is NTGC which is described in detailes in chapter 1. Below, we give descriptions of some of the important commands listed in Figure 4.1.

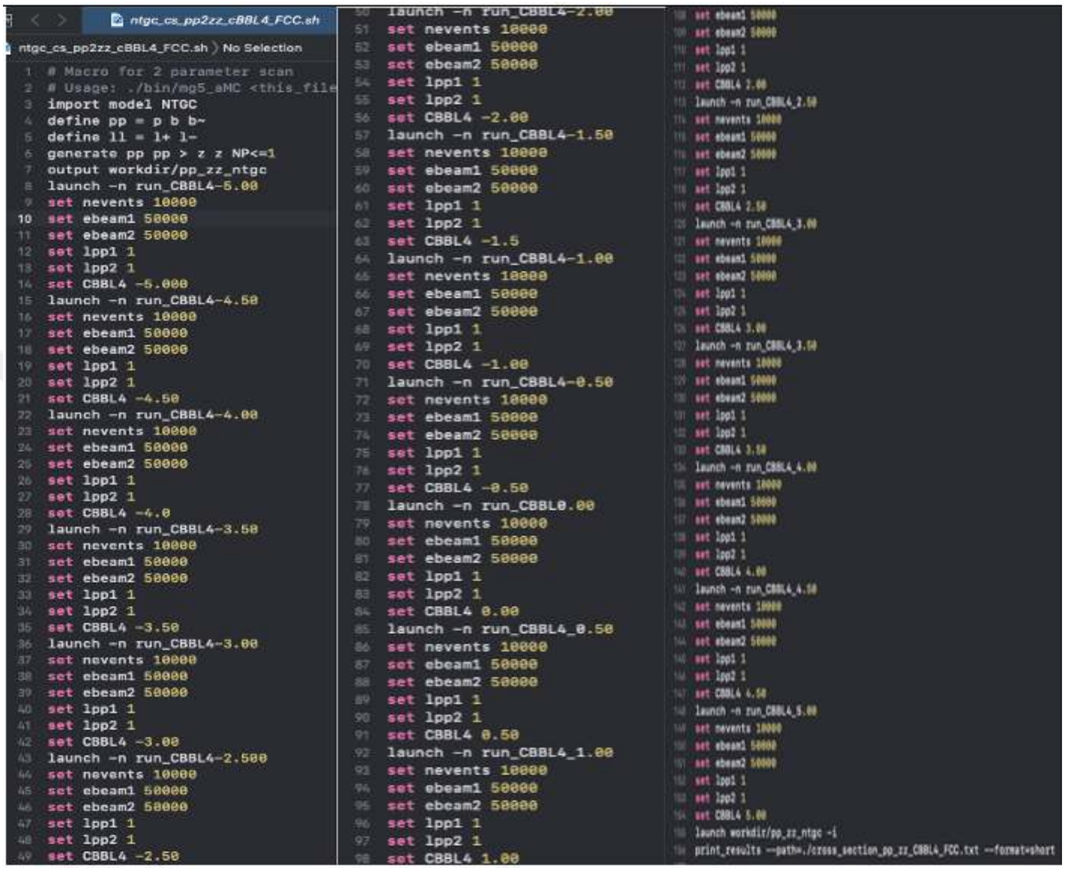

```
ntgc_cs_pp2zz_cBBL4_FCC.sh
ntgc_cs_pp2zz_cBBL4_FCC.sh 〉 No Selection
# Macro for 2 parameter scan
# Usage: ./bin/mg5_aMC <this_file
import model NTGC
define pp = p b b~
define ll = l+ l-
generate pp pp > z z NP<=1
output workdir/pp_zz_ntgc
launch -n run_CBBL4-5.00
set nevents 10000
set ebeam1 50000
set ebeam2 50000
set lpp1 1
set lpp2 1
set CBBL4 -5.000
launch -n run_CBBL4-4.50
set nevents 10000
set ebeam1 50000
set ebeam2 50000
set lpp1 1
set lpp2 1
set CBBL4 -4.50
launch -n run_CBBL4-4.00
set nevents 10000
set ebeam1 50000
set ebeam2 50000
set lpp1 1
set lpp2 1
set CBBL4 -4.0
launch -n run_CBBL4-3.50
set nevents 10000
set ebeam1 50000
set ebeam2 50000
set lpp1 1
set lpp2 1
set CBBL4 -3.50
launch -n run_CBBL4-3.00
set nevents 10000
set ebeam1 50000
set ebeam2 50000
set lpp1 1
set lpp2 1
set CBBL4 -3.00
launch -n run_CBBL4-2.500
set nevents 10000
set ebeam1 50000
set ebeam2 50000
set lpp1 1
set lpp2 1
set CBBL4 -2.50
launch -n run_CBBL4-2.00
set nevents 10000
set ebeam1 50000
set ebeam2 50000
set lpp1 1
set lpp2 1
set CBBL4 -2.00
launch -n run_CBBL4-1.50
set nevents 10000
set ebeam1 50000
set ebeam2 50000
set lpp1 1
set lpp2 1
set CBBL4 -1.5
launch -n run_CBBL4-1.00
set nevents 10000
set ebeam1 50000
set ebeam2 50000
set lpp1 1
set lpp2 1
set CBBL4 -1.00
launch -n run_CBBL4-0.50
set nevents 10000
set ebeam1 50000
set ebeam2 50000
set lpp1 1
set lpp2 1
set CBBL4 -0.50
launch -n run_CBBL0.00
set nevents 10000
set ebeam1 50000
set ebeam2 50000
set lpp1 1
set lpp2 1
set CBBL4 0.00
launch -n run_CBBL4_0.50
set nevents 10000
set ebeam1 50000
set ebeam2 50000
set lpp1 1
set lpp2 1
set CBBL4 0.50
launch -n run_CBBL4_1.00
set nevents 10000
set ebeam1 50000
set ebeam2 50000
set lpp1 1
set lpp2 1
set CBBL4 1.00
set ebeam1 50000
set ebeam2 50000
set lpp1 1
set lpp2 1
set CBBL4 2.00
launch -n run_CBBL4_2.50
set nevents 10000
set ebeam1 50000
set ebeam2 50000
set lpp1 1
set lpp2 1
set CBBL4 2.50
launch -n run_CBBL4_3.00
set nevents 10000
set ebeam1 50000
set ebeam2 50000
set lpp1 1
set lpp2 1
set CBBL4 3.00
launch -n run_CBBL4_3.50
set nevents 10000
set ebeam1 50000
set ebeam2 50000
set lpp1 1
set lpp2 1
set CBBL4 3.50
launch -n run_CBBL4_4.00
set nevents 10000
set ebeam1 50000
set ebeam2 50000
set lpp1 1
set lpp2 1
set CBBL4 4.00
launch -n run_CBBL4_4.50
set nevents 10000
set ebeam1 50000
set ebeam2 50000
set lpp1 1
set lpp2 1
set CBBL4 4.50
launch -n run_CBBL4_5.00
set nevents 10000
set ebeam1 50000
set ebeam2 50000
set lpp1 1
set lpp2 1
set CBBL4 5.00
launch workdir/pp_zz_ntgc -i
print_results --path=./cross_section_pp_zz_CBBL4_FCC.txt --format=short
```

Figure 4.1. Shell script to scan C_{BB}/Λ^4 coupling (*ntgc_cs_pp2zz_cBB4_FCC.sh*).

The first line in the shell script imports the model NTGC: *import model NTG*. Following three lines are used to define the particles and define the process to start generation: *define pp = p b b~* (here the b/ $\bar{b}$ are added to the multiparticle labels), *define ll = l^+ l^-*, and *generate pp pp > zz NP<=1*. The directory where the MadGraph puts all related output files is defined with a command: output *workdir/pp_zz_ntgc*.

launch -n run_CBBL4-5.00 command launches event generation or matrix element evaluation for created process directories. The number of unweighted events requested is defined with *set nevents 10000* where we generate 10k events. Beam energy and type are set with the following 4 lines in the script: *set ebeam1 50000* (beam 1 total energy in GeV), *set ebeam2 50000* (beam 2 total energy in

GeV), *set lpp1 1* and *set lpp2 1* (1 tells MadGraph to use a beam of colliding protons). *set CBBL4 -5.000* command sets all couplings to zero except C_{BB}/Λ^4 coupling which is set to -5.000 TeV^{-4}. Finally, results of the cross secions are written in the file cross_section_pp_zz_CBBL4_FCC.txt with a command *print_results --path=./cross_section_pp_zz_CBBL4_FCC.txt --format=short.*

4.2 Cross sections for $pp \rightarrow ZZ$

Searches for neutral triple gauge boson couplings, which are known to be forbidden in the SM at tree-level, can be utilized through the production of two Z gauge bosons. It is well-known that triple Z gauge boson interactions are significant probes for both new sources of CP violation in new physics beyond the SM and new particle thresholds. Measurements of triple Z boson interactions in the literature are carried out in the frameworks of anomalous couplings and effective field theory.

The high center of mass energy of the LHC provides a good environment to search for such interactions. In this study we derive possible bounds on NTGC of ZZ diboson production, at a set of different planned future colliders, in the framework of the EFT. We generated the signal and the background events for the pp → ZZ process by importing the signal NTGC implemented through UFO model file into MadGraph5_aMC@NLO v2.6.4 (65). For parton showering and hadronization, the package PYTHIA v8.2 (73) has been used. LHAPDF v6.1.6 (67) library and its NNPDF v2.3 (68) set is used as the default set of parton distribution functions (PDFs) for all simulated MC samples. Events of the signal and the background were generated for each dim-8 effective coupling. For each collider involved in this investigation, the detector response is simulated using a detailed description of each collider detector card implemented in the Delphes v3.4.1 (69). The analysis of all events is carried out through using the ExRootAnalysis (70) package with ROOT v6.16 (71). For a given collider, the kinematical distributions have been normalized to the number of expected events that is defined as the cross section of each processes including the branching fraction times integrated luminosity. Feynman diagrams contributing to the signal and its main-background processes are displayed in Figure 4.2 (a) and Figure 4.2 (b), respectively. In the figure, the red dot stands for the NTGC vertex in the production of ZZ.

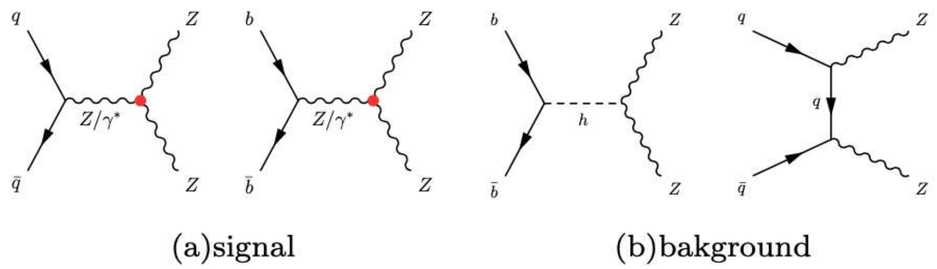

Figure 4.2. Feynman diagrams of ZZ production (a) for signal including an aNTGC vertex depicted by a red dot, (b) for the SM background.

In the presence of SM extensions parameterized by the operators listed in Eqs. (1.29-1.32), it is direct to see that the operators with dimension six cannot generate neutral gauge couplings at tree-level. However, they can contribute to nTGC at one-loop level with contributions of order $\frac{\propto_{EM}}{4\pi}\frac{S}{\Lambda^2}$. This has to be compared with the contributions originating, at tree-level, from operators with dimension equal to eight of order $\frac{sv^2}{\Lambda^4}$. Clearly, the contributions of the dimension-eight operators are the dominant ones for an energy scale given by $\Lambda \lesssim \sqrt{\frac{4\pi}{\propto_{EM}}}\ s \approx 10$TeV. As a result, large new physics contribution to the amplitude of $f\bar{f} \rightarrow$ ZZ is expected to originate from the interference between the SM and dimension-eight operators given in Eqs. (1.29-1.32). Hence, the square of the amplitude, necessary for the calculation of the cross section, of the process $f\bar{f} \rightarrow$ ZZ can be expressed as

$$|M|^2 = |M_{SM}|^2 + 2R(M_{SM}M^*_{dim8}) + |M_{dim8}|^2 + \cdots + O(\Lambda^{-10}). \tag{4.1}$$

In the calculations of the cross section a set of generator level cuts has been adopted; a lepton is declared to be isolated if the p_T - sum of all particles within the isolation cone size Riso = 0.3, minimum $p_T = 10$ GeV and $|\eta| < 2.5$ for the charged leptons. Additionally, in the calculations, the default Z mass is set to be 91.187 GeV.

The cross sections of $pp \rightarrow ZZ$ production as a function of the four dim-8 couplings are displayed in Figure 4.3. It should be noted that, in the figure, for the plot of the cross sections we vary one coupling each time in the range of the limits reported by CMS collaboration (74) while other couplings are set to zeros. Clearly, from the plots in the figure, there is notable deviation of the cross sections in the presence of new physics from the SM cross section which can be calculated from the figure by setting the coupling to zero.

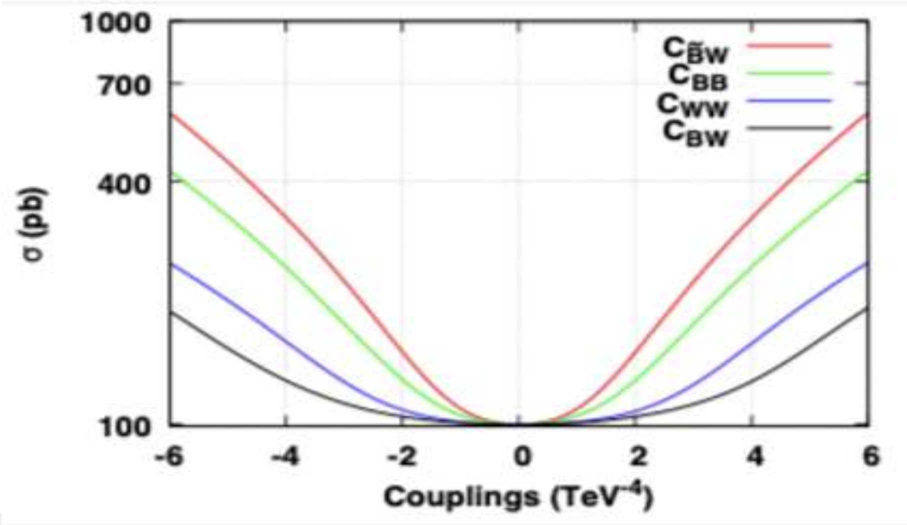

Figure 4.3. Cross sections for the process with NTGCs including CP-conserving and CP-violating terms in the Lagrangian.

In Figure 4.4. we plot cross section of $pp \rightarrow ZZ$ as a function of the different effective couplings C_{BB}/Λ^4, $C_{\tilde{B}W}/\Lambda^4$, C_{BW}/Λ^4 and C_{WW}/Λ^4 in the range between $-6\,TeV^{-4}$ and $6\,TeV^{-4}$ at FCC-hh future circular collider where the solid line represents the fit function and the points represent the data. In each plot only one coupling is nonzero while others are set to zero. As can be seen from the figure, the cross section varies between 100 pb and higher values greater than 100 pb for all the couplings C_{BB}/Λ^4, $C_{\tilde{B}W}/\Lambda^4$, C_{BW}/Λ^4 and C_{WW}/Λ^4 in the ranges under consideration. The SM cross section ($\sigma_{SM} = 100$) can be obtained from any plot by setting the coupling to zeros. One can remark from the figure that, the cross-section is more sensitive to C_{BB}/Λ^4 and $C_{\tilde{B}W}/\Lambda^4$ couplings than C_{BW}/Λ^4 and C_{WW}/Λ^4.

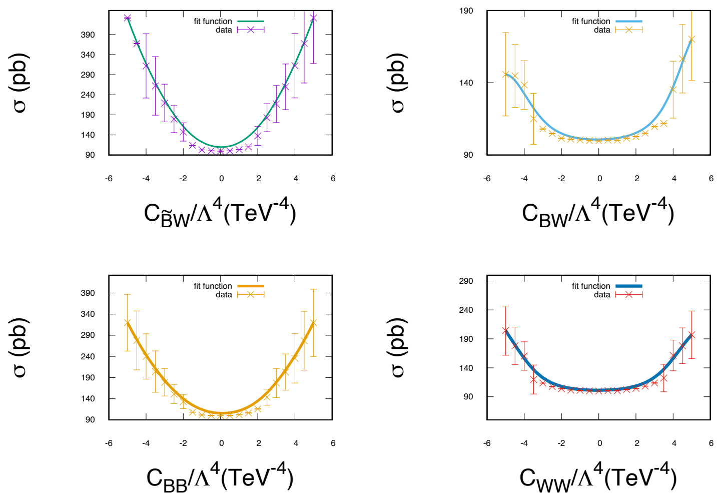

Figure 4.4. The cross section of $pp \rightarrow ZZ$ as a function of different effective couplings at FCC-hh with center of mass energy of 100 TeV.

We turn now to show our results for the cross section of $pp \rightarrow ZZ$ as a function of the effective couplings C_{BB}/Λ^4, $C_{\tilde{B}W}/\Lambda^4$, C_{BW}/Λ^4 and C_{WW}/Λ^4 at HL-LHC future circular collider. This is displayed in Figuer 4.5 where, as in the previous figure, the solid line represents the fit function and the x crosses represent the data. We can see from the plot in the top left in the figure that the dominant contribution to the cross section comes from the effective coupling $C_{\tilde{B}W}/\Lambda^4$. we note also from the plots in the up right and the down right in the figures that, the cross sections are not affected notably by the values of the effective couplings C_{BW}/Λ^4 and C_{WW}/Λ^4.

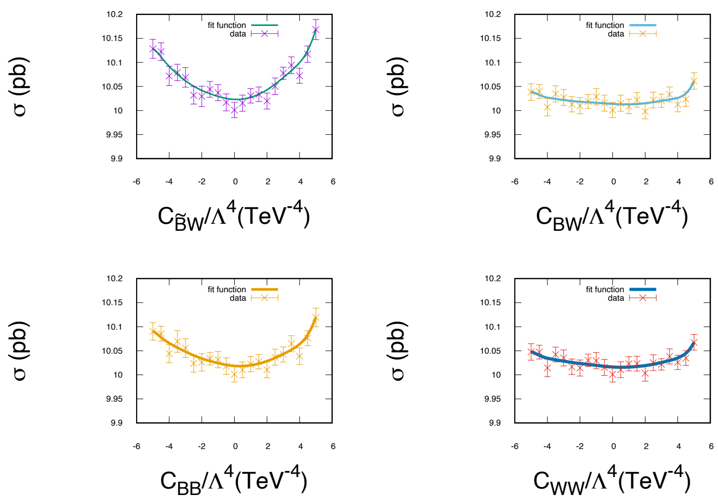

Figure 4.5. The cross section of $pp \rightarrow ZZ$ as a function of different effective couplings at HL-LHC with $\sqrt{s}$=14 TeV.

We move to Figure 4.6 in which we present the change of the cross section of the $pp \rightarrow ZZ$ diboson production as a function of the effective couplings C_{BB}/Λ^4, $C_{\tilde{B}W}/\Lambda^4$, C_{BW}/Λ^4 and C_{WW}/Λ^4 for the future LE-FCC circular collider. As in the previous figures, the solid line represents the fit function and the x crosses represent the data. Clearly, from the top left and bottom left plots in the figure, that the main contributions to the cross sections come from the effective couplings $C_{\tilde{B}W}/\Lambda^4 and\ C_{BB}/\Lambda^4$ while other couplings do not contribute effectively to the cross sections.

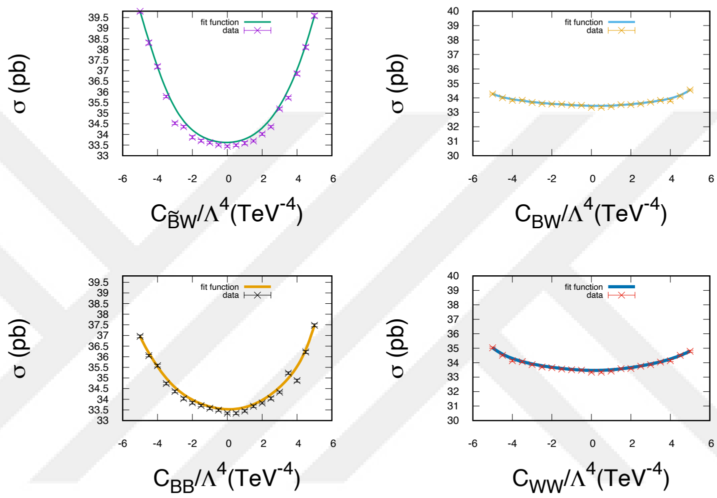

Figure 4.6. The cross section of $pp \rightarrow ZZ$ as a function of different effective couplings at LE-FCC with center of mass energy of 37.5 TeV.

Figure 4.7, given below, corresponds to our results of the variation of the cross section of $pp \rightarrow ZZ$ with the different effective couplings C_{BB}/Λ^4, $C_{\tilde{B}W}/\Lambda^4$, C_{BW}/Λ^4 and C_{WW}/Λ^4 at HE-LHC future circular collider. As stated above, the solid line represents the fit function and the x crosses represent the data. As in the previous figure, one can notice that the dominant contributions to the cross sections arise from the effective couplings $C_{\tilde{B}W}/\Lambda^4 and\ C_{BB}/\Lambda^4$ while the other couplings have small impact on the cross sections.

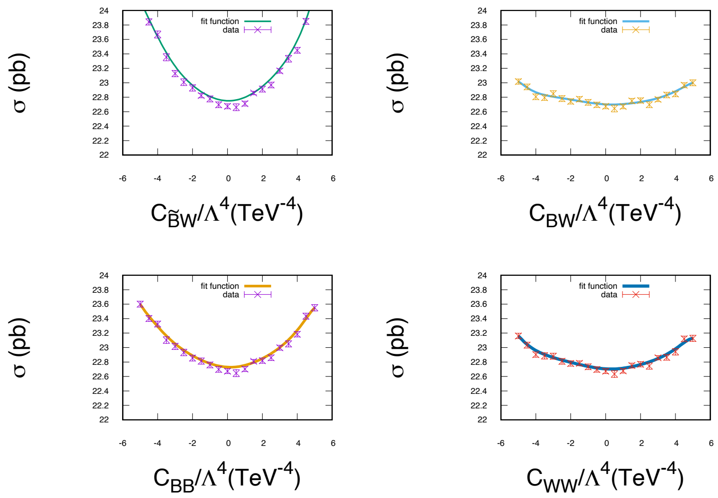

Figure 4.7. The cross section of $pp \rightarrow ZZ$ as a function of different effective couplings at HE-LHC with center of mass energy of 27 TeV.

In the previous figures, we displayed separately the plots of the cross sections of $pp \rightarrow ZZ$ for a given collider. For comparison, we show in Figure 4.8, the plots of the variation of the cross sections of $pp \rightarrow ZZ$ with the center of mass energy for a group of possible future circular colliders. These cross sections are plotted for representative values of the couplings taken as $C_{BB}/\Lambda^4 = 2.5\,TeV^{-4}$ in yellow color, $C_{\tilde{B}W}/\Lambda^4 = 2.5\,TeV^{-4}$ in green color, $C_{BW}/\Lambda^4 = 2.5\,TeV^{-4}$ in black color, $C_{WW}/\Lambda^4 = 2.5\,TeV^{-4}$ in red color and the blue solid line represents the SM cross section. It should be noted that the center of mass energy $\sqrt{s}$ = 14TeV, 27TeV, 37.5TeV and 100TeV correspond to HL-LHC, HE-LHC, LE-FCC, and FCC-hh future colliders respectively. We note from the figure, that the cross sections in LE-FCC, HL-LHC, HE-LHC colliders are the same as the SM one regardless the values of the effective couplings. For center of mass energy equals 40 TeV, the cross sections start to be different than the SM cross section for the selected values of the effective couplings. This difference is maximum at center of mass energy 100 TeV which corresponds to FCC-hh collider. Finally, from the figure, we see that the dominant contribution to the cross sections comes from the effective coupling $C_{\tilde{B}W}/\Lambda^4$ as can be noticed from the green solid line.

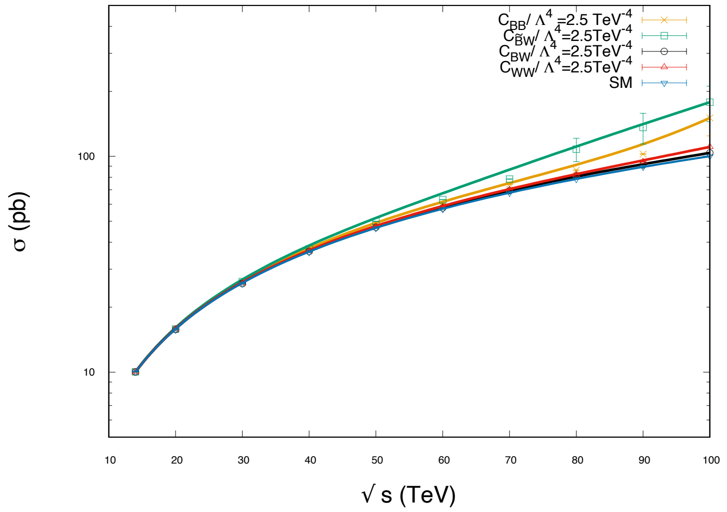

Figure 4.8. The cross section as a function of the center of mass energy for possible future circular collider where the different colors represent different effective couplings and the blue solid line represents the SM cross section.

4.3 Kinematic variables distributions

In order to show the distributions of the kinematic variables of the final state particles, we generate the events with $C_{\tilde{B}W}/\Lambda^4$ = 30TeV^4 (set all the other couplings to zero) as a signal and SM background with the same final state via Madgraph for FCC-hh collider at center of mass energy100 TeV. Events passed through PYTHIA for hadronization and realistic detector effects are included with Delphes. Distributions are discussed in the following subsections where one of the Z bosons decays to $\nu\nu$ and the other Z decays to e^+e^-, $\mu^+\mu^-$ and $q\,\bar{q}$ as in subsections 4.3.1, 4.3.2 and 4.3.3, respectively. In all figures shown in this section, the red solid line represents the signal for $C_{\tilde{B}W}/\Lambda^4 = 30\text{TeV}^4$ while the black solid line represents the SM.

4.3.1 $e^+e^-\nu_e\bar{\nu}_e$ final state

In this subsection, we demonstrate the behavior of the kinematic variables of the final state particles such as transverse momentum $p_T^{e_i}$, rapidity (η^{e_i}), Missing Energy Transfer and invariant mass of Z boson reconstructed from the oppositely charged leading and sub-leading electrons.

In Figure 4.9 we plot the transverse momentum and pseudo-rapidity of leading (top) and sub-leading (bottom) electrons. From these figures, the behavior for both SM and signal looks very similar.

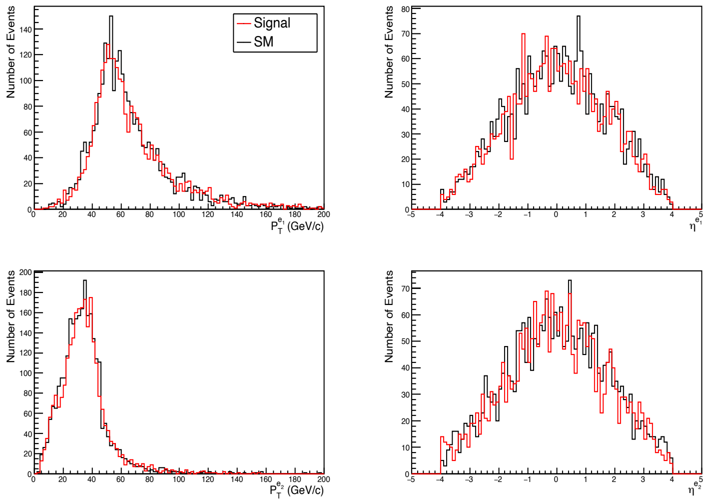

Figure 4.9. Kinematic distributions of leading (top row) and sub-leading (bottom row) electrons for the process $pp \longrightarrow e^+e^-\nu_e\bar{\nu}_e$: the transverse momentum $p_T^{e_i}$ (left) and rapidity η^{e_i} (right).

For the process $pp \longrightarrow e^+e^-\nu_e\bar{\nu}_e$, the distributions of the Missing Energy Transfer and the invariant mass of Z boson reconstructed by the two oppositely charged leading electrons are presented in Figure 4.10 we remark from the plots in the same figure that, the signal and SM show similar patterns to each other.

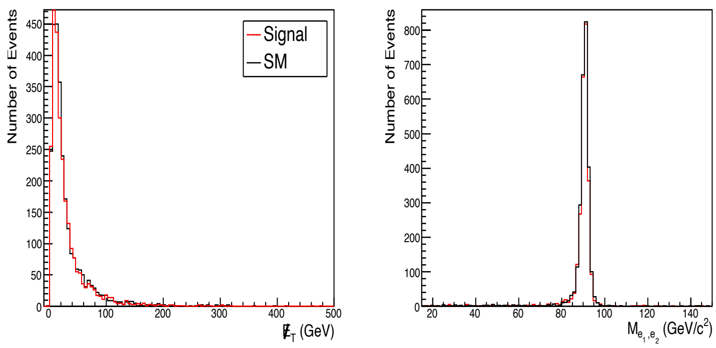

Figure 4.10. Distribution of Missing Energy Transfer (left) and invariant mass of Z boson (right) reconstructed by the two oppositely charged leading electrons for the process $pp \longrightarrow e^+e^-\nu_e\bar{\nu}_e$.

The 2-Dimensional plots of the kinematic variables Missing Energy Transfer, transverse momentum of the leading and sub-leading electrons versus invariant mass of Z boson reconstructed by the two oppositely charged leading electrons are shown in Figure 4.11. In the figure**,** the plots in the top row correspond to the signal while the plots in the bottom row correspond to SM background. As can be seen from these plots, points populate around the mass of Z boson (90 GeV/c^2). In addition, the transverse momentum of the leading electron starts from approximately 30 GeV/c^2 while the transverse momentum of the sub-leading electron starts to contribute to Z boson from 10 GeV/c^2. Another remark from the figure that, both SM and signal behave similarly.

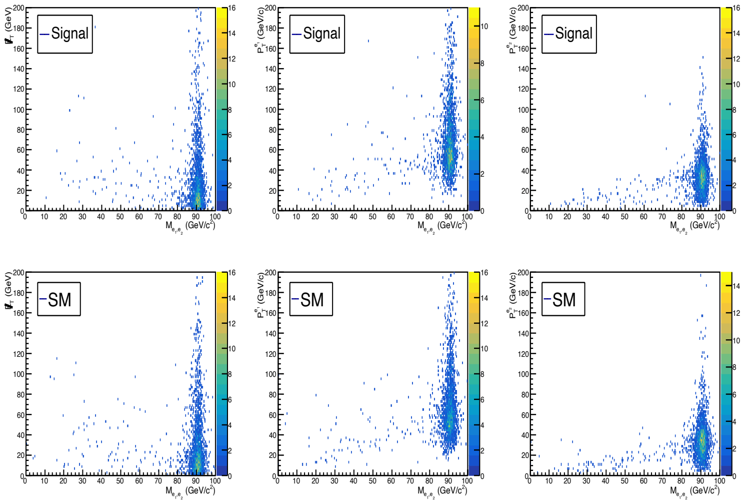

Figure 4.11. Missing energy transfer, transverse momentum of the leading electron and sub-leading electrons as a function of invariant mass of Z boson reconstructed by two oppositely charged leading electrons (left to right, respectively). The distributions correspond to the process $pp \longrightarrow e^+e^-\nu_e\bar{\nu}_e$.

In Figure 4.12 we plot the distribution of the transverse momentum of Z boson (top left), cos θ^z (top right), polar angle of the Z boson in the center of mass system (down to the left) and the angular distance separating the electrons (down to the right) for the process $pp \longrightarrow e^+e^-\nu_e\bar{\nu}_e$. We note from the figure that, the plots of the signal and SM are nearly identical to each other in most of the ranges of the variables. This means that these variables will not help to reveal the impact of new physics in this process. It should be noted that, in the $\eta - \phi$ *plan* $\Delta R^{e_1,e_2}$ is defined as $\Delta R^{e_1,e_2} = \sqrt{(\eta^{e_1} - \eta^{e_2})^2 + (\phi^{e_1} - \phi^{e_2})^2}$. (4.2)

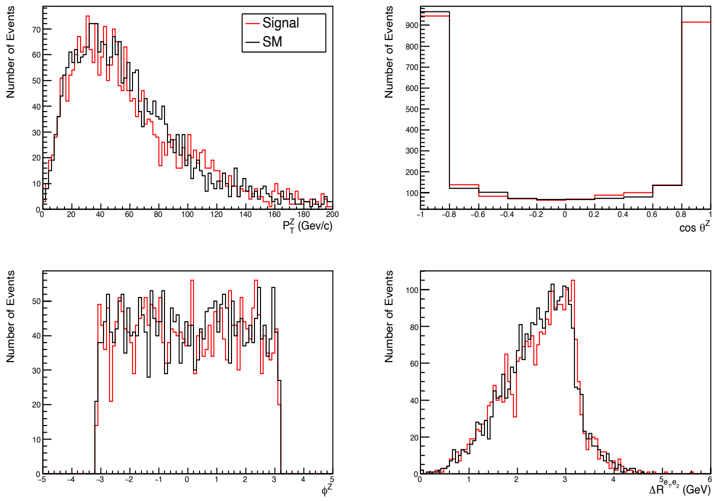

Figure 4.12. The distribution of transverse momentum of Z boson (top left), cos θ^z (top right), polar angle of the Z boson in the center of mass system (down to the left) and the angular distance separating the electrons (down to the right) for the process $pp \longrightarrow e^+e^-\nu_e\bar{\nu}_e$.

4.3.2 $\mu^+\mu^-\nu_\mu\bar{\nu}_\mu$ final state

The following analysis for the process $pp \longrightarrow \mu^+\mu^-\nu_\mu\bar{\nu}_\mu$ will be carried out in a similar way to the one performed for the process $pp \longrightarrow e^+e^-\nu_e\bar{\nu}_e$. We show in this subsection, the patterns of the kinematic variables of the final state particles related to the process $pp \longrightarrow \mu^+\mu^-\nu_\mu\bar{\nu}_\mu$ in Fig4.13, Fig4.14, Fig4.15 and Fig4.16. As before, the kinematic variables include the transverse momentum of the muons, $p_T^{\mu_i}$, rapidity (η^{μ_i}), Missing Energy Transfer and invariant mass of Z boson reconstructed from the oppositely charged leading (i =1) and sub-leading muons (i =2).

In Figure 4.13 we plot the kinematic distributions, particularly the transverse momentum and rapidity of the muons, of the leading (top row) and subleading (bottom row) muons in the process $pp \longrightarrow \mu^+\mu^-\nu_\mu\bar{\nu}_\mu$. We can deduce from the figure that, both SM and signal follow nearly similar patterns.

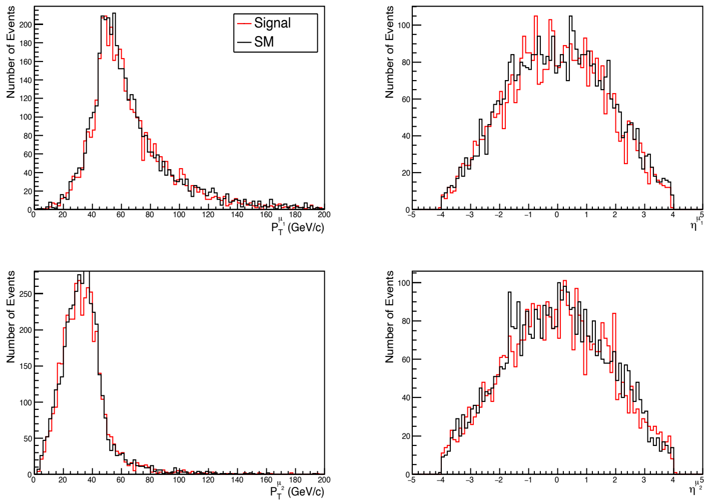

Figure 4.13. Kinematic distributions of leading (up row) and sub leading (down row) muons for the process $pp \longrightarrow \mu^+\mu^-\nu_\mu\bar{\nu}_\mu$: the transverse momentum $p_T^{\mu_i}$ (left) and rapidity η^{μ_i} (right).

We present in Figure 4.14 the plots of the distributions of the Missing Energy Transfer and the invariant mass of the Z boson reconstructed from the two oppositely charged leading and sub-leading muons for the process $pp \longrightarrow \mu^+\mu^-\nu_\mu\bar{\nu}_\mu$. We note from the figure that, the plots of the distributions of the signal and the SM are almost the same indicating that the effect of the assigned value of the coupling, $C_{\tilde{B}W}/\Lambda^4 = 30\text{TeV}^4$, on the signal is so small.

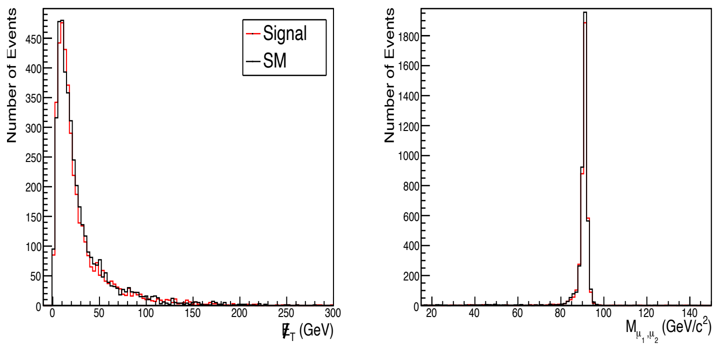

Figure 4.14. Distribution of Missing Energy Transfer (left) and invariant mass of Z boson (right) reconstructed by two oppositely charged leading muons for the process $pp \longrightarrow \mu^+\mu^-\nu_\mu\bar{\nu}_\mu$.

We display in Figure 4.15 the 2- Dimensional plots of the variation of the kinematic variables, namely the Missing Energy Transfer, the transverse momentum of the leading muon and the transverse momentum of the sub-leading muons with the invariant mass of Z boson reconstructed from the two oppositely charged leading muons**.** In the same figure**,** the top row plots represent the signal while bottom row plots show the SM background. It is clear from the figure that; points accumulate around the mass of the Z boson. Moreover, we notice from the figure that transverse momentum of the leading muon begins to contribute from 30 GeV/c^2 while the transverse momentum of the sub-leading muon is contributing to the Z boson nearly from 10 GeV/c^2. Again, as in the case of $e^+e^-\nu_e\bar{\nu}_e$ final state, plots of both SM and signal are quite similar.

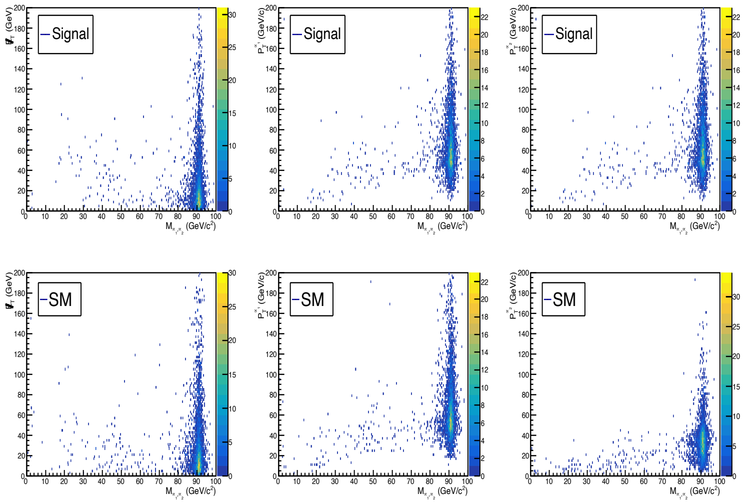

Figure 4.15. Missing Energy Transfer, transverse momentum of the leading muon and sub-leading muon as a function of invariant mass of Z boson reconstructed by two oppositely charged leading muons (left to right, respectively). The distributions correspond to the process $pp \longrightarrow \mu^+\mu^-\nu_\mu\bar{\nu}_\mu$.

In Figure 4.16 we show our results for the distributions of the transverse momentum of Z boson (top left), cos θ^z (top right), polar angle of the Z boson in the center of mass system (down to the left) and the angular distance between the two muons (down to the right) in the process $pp \longrightarrow \mu^+\mu^-\nu_\mu\bar{\nu}_\mu$. It is clear from the figure that, for most considered values of the parameters, the variation of the signal follows pattern close to that of the SM one. One should remark that, the angular distance between the two muons, in the $\eta - \phi$ plane, $\Delta R^{\mu_1,\mu_2}$ is defined as

$$\Delta R^{\mu_1,\mu_2} = \sqrt{(\eta^{\mu_1} - \eta^{\mu_2})^2 + (\phi^{\mu_1} - \phi^{\mu_2})^2}. \quad (4.3)$$

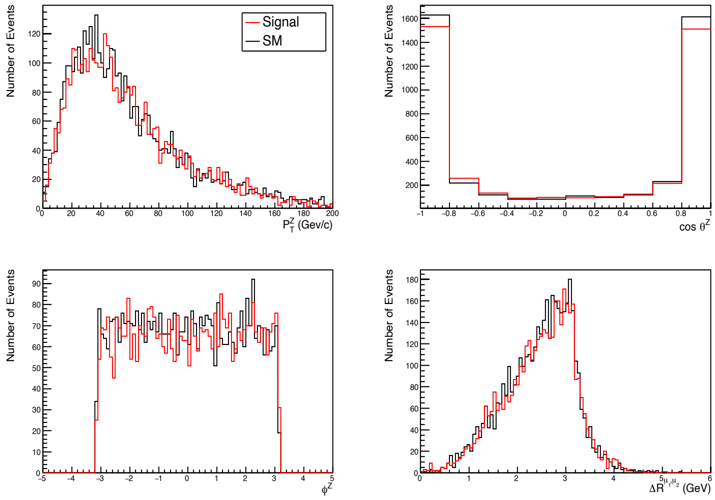

Figure 4.16. The distribution of transverse momentum of Z boson (top left), cos θ^{z} (top right), polar angle of the Z boson in the center of mass system (down to the left) and the angular distance separating the muons (down to the right) related to the process $pp \longrightarrow \mu^{+}\mu^{-}\nu_{\mu}\bar{\nu}_{\mu}$.

4.3.3 $qq\ \nu\bar{\nu}$ final state

We proceed to investigate the kinematic variables of the final state particles for both SM and signal regarding the process $pp \longrightarrow qq\ \nu\bar{\nu}$. These investigations are presented in Fig 4.17, Fig 4.18, Fig 4.19 and Fig 4.20. As in the previous subsections, we mainly consider the transverse momentum $p_T^{q_i}$, rapidity η^{q_i} of the leading (i=1) and sub-leading (i=2) jets, Missing Energy Transfer and invariant mass of Z boson reconstructed from the oppositely charged leading and sub-leading jets.

We start our discussion by showing in Figure 4.17 the plot of the kinematic distributions, the transverse momentum and pseudo-rapidity, of the leading (top row) and sub-leading (bottom row) jets. As can be seen from the figure, both SM and signal lead to approximate same predictions for the studied kinematic variables.

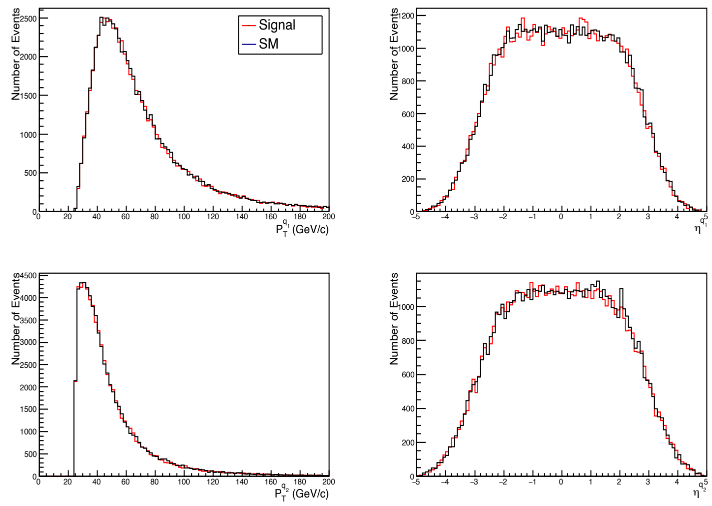

Figure 4.17. Kinematic distributions of leading (up row) and sub leading (down row) jets for the process $pp \longrightarrow qq\, \nu\bar{\nu}$: the transverse momentum $p_T^{q_i}$ (left) and rapidity η^{q_i} (right).

Considering other kinematic variables, we present in Figure 4.18 the distributions of Missing Energy Transfer and the invariant mass of Z boson reconstructed from the two oppositely charged leading and sub-leading jets. We can easily remark that, from the plots in the figure, the variations of the distributions follow the same patterns for the signal and SM.

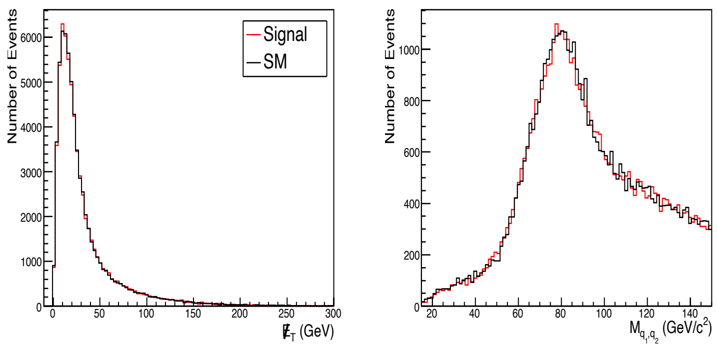

Figure 4.18. Distribution of Missing Energy Transfer (left) and invariant mass of Z boson (right) reconstructed by two oppositely charged leading and sub-leading jets for the process $pp \longrightarrow qq\, \nu\bar{\nu}$.

We turn now to Figure 4.19 in which we display the 2- Dimensional plots of the changes in the kinematic variables namely, the Missing Energy Transfer, the transverse momentum of the leading jet and the transverse momentum of the sub-leading jet as a function of the invariant mass of the Z boson reconstructed by two oppositely charged quarks forming the two jets**.** In the top row part of the figure**,** we show the signal while the bottom row part is devoted to the SM background.

Clearly from the figure that; points do not accumulate around the mass of Z boson as observed in the cases of the $e^+e^-\nu_e\bar{\nu}_e$ and $\mu^+\mu^-\nu_\mu\bar{\nu}_\mu$ final states but rather spread over a range starting approximately from 50 GeV/c^2 to 100 GeV/c^2. In addition, as one can notice from the figure that, SM and signal yield quite similar distributions.

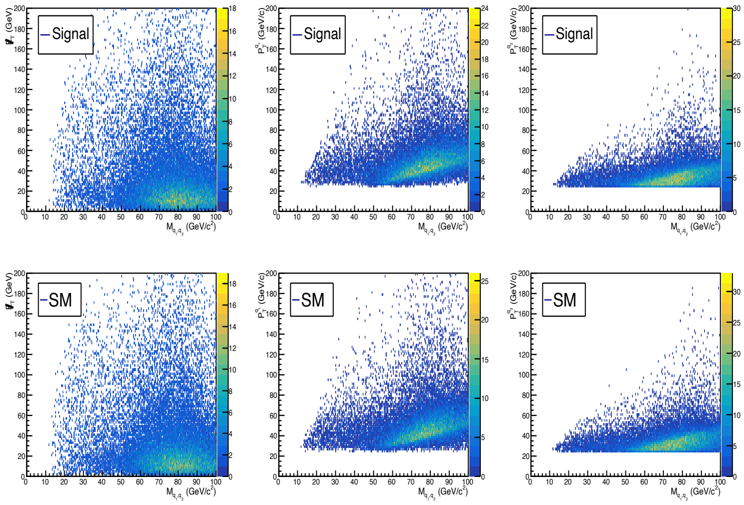

Figure 4.19. Missing Energy Transfer, transverse momentum of the leading muon and subleading jets as a function of invariant mass of Z boson reconstructed by two oppositely charged leading jets (left to right, respectively). The distributions correspond to the process $pp \longrightarrow qq\,\nu\bar{\nu}$.

We end this subsection by displaying in Figure 4.20 the plots of the distributions of the transverse momentum of Z boson (top left), cos θ^z (top right), polar angle of the Z boson in the center of mass system (bottom left) and the angular distance between the two jets (bottom right) for the process $pp \longrightarrow qq\,\nu\bar{\nu}$. The definition of ΔR is similar to the corresponding ones of the electrons and muons but here we use q_1 and q_2 instead of electrons and muons. It turns out that the distributions of the signal and the SM are closely similar to each other over the whole range of each parameter in the figure.

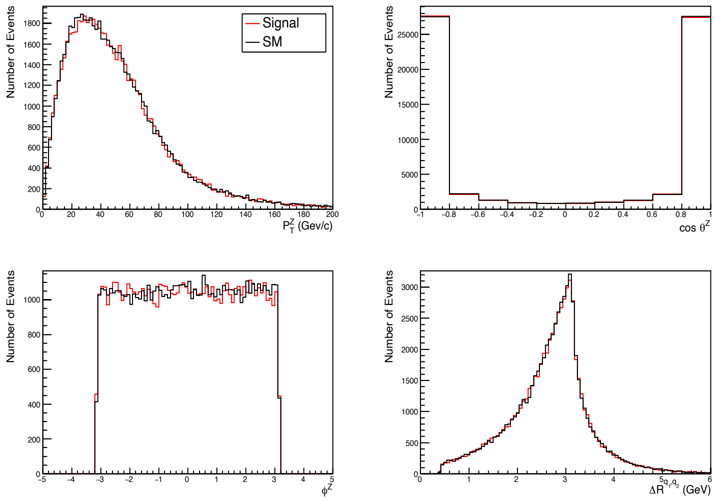

Figure 4.20. The distribution of transverse momentum of Z boson (top left), cos θ^z (top right), polar angle of the Z boson in the center of mass system (down to the left) and the angular distance separating the jets (down to the right) corresponding to the process $pp \longrightarrow qq\ \nu\bar{\nu}$.

4.4 Sensitivity

In the literature, one of the well-known methods to show the sensitivities of the couplings is to apply χ^2 criterion. The χ^2 function is defined as follows:

$$\chi^2 = \left(\frac{\sigma^{signal} - \sigma^{SM}}{\sigma^{SM} \cdot \delta_i}\right)^2 \tag{4.4}$$

Where σ^{signal} is the cross section in the presence of anomalous couplings, σ^{SM} is the cross section of the SM background and δ is the statistical error defined as $\delta_i = \frac{1}{\sqrt{N_i}}$ with i runs over $\ell\ell\nu\nu$, $qq\nu\nu$, $\ell\ell qq$ and $\ell\ell\,\ell\ell$. The factor N_i is given by

$$N_{\ell\ell\nu\nu} = \sigma_{SM} \,.\, L_{int} \,.\, BR(Z \longrightarrow \ell\ell) \,.\, BR(Z \longrightarrow invisible). \tag{4.5}$$

$$N_{qq\nu\nu} = \sigma_{SM} \,.\, L_{int} \,.\, BR(Z \longrightarrow qq) \,.\, BR(Z \longrightarrow invisible). \tag{4.6}$$

$$N_{\ell\ell qq} = \sigma_{SM} . L_{int} . BR(Z \longrightarrow \ell\ell) . BR(Z \longrightarrow qq). \tag{4.7}$$

$$N_{\ell\ell\,\ell\ell} = \sigma_{SM} . L_{int} . BR(Z \longrightarrow \ell\ell) . BR(Z \longrightarrow \ell\ell). \tag{4.8}$$

where L_{int} is the integrated luminosity and BR is the branching ratios of the given decay mode of Z boson. The branching ratios related to our study are listed in Table 4.1.

Table 4.1. Branching ratios of the decay modes of Z boson relevant to our studied processes (PDG).

Decay mode	BR (branching ratios)
$Z \longrightarrow \ell\ell$	(3.3632±0.0042) %
$Z \longrightarrow qq$(hadrons)	(69.911 ±0.056) %
$Z \longrightarrow invisible$	(20.000 ±0.055) %
$Z \longrightarrow e^+e^-$	(3.3632±0.0042) %
$Z \longrightarrow \mu^+\mu^-$	(3.3662±0.0066) %

In this thesis, we are interested in obtaining the 95% confidence level (CL) limits on the effective couplings C_{BB}/Λ^4, $C_{\tilde{B}W}/\Lambda^4$, C_{BW}/Λ^4 and C_{WW}/Λ^4 for the mentioned future colliders in chapter 2. We derive these limits using χ^2 function defined in Eq. (4.4).

The χ^2 as a function of the different effective coupling C_{BB}/Λ^4, $C_{\tilde{B}W}/\Lambda^4$, C_{BW}/Λ^4 and C_{WW}/Λ^4 for the process $pp \longrightarrow ZZ \longrightarrow \ell\ell\nu\nu$ is plotted for a 100 TeV center of mass energy machine FCC-hh with an integrated luminosity of 30 ab^{-1} in Figuer 4.21. The Blue solid line represents the χ^2 function while the orange line represents a specific value χ^2 =3.84. The intersection points between the blue and orange lines in the figure give the 95% C.L. limits for the couplings. Consequently, these limits for C_{BB}/Λ^4 , $C_{\tilde{B}W}/\Lambda^4$, C_{BW}/Λ^4 and C_{WW}/Λ^4 are obtained as [-0.38;0.38], [-0.30;0.31], [-0.73;0.73] and [-0.56;0.56] respectively. These limits are summarized in table 5.1. in the next chapter.

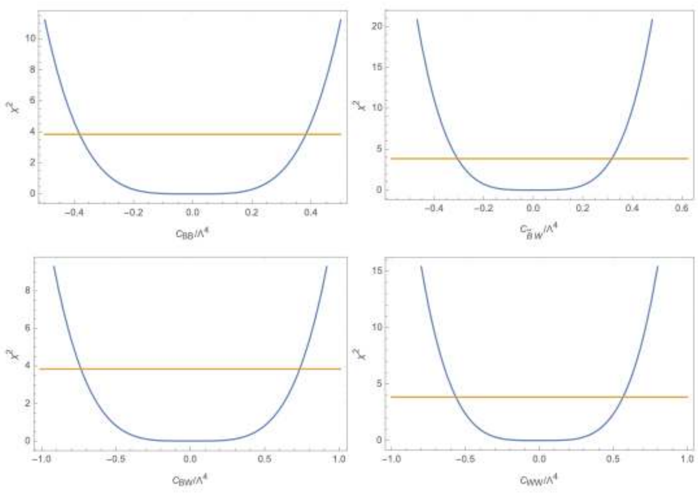

Figure 4.21. χ^2 (Blue solid line) as a function of the different effective couplings C_{BB}/Λ^4, $C_{\tilde{B}W}/\Lambda^4$, C_{BW}/Λ^4 and C_{WW}/Λ^4 for the process $pp \longrightarrow ZZ \longrightarrow \ell\ell\nu\nu$ at FCC-hh while the orange line represents χ^2 =3.84.

Different final states processes resulted from the decays of the Z boson have been studied in this thesis. Among them is the processes $pp \longrightarrow ZZ \longrightarrow \ell\ell\ell\ell$ for which the χ^2 as a function of the different effective coupling C_{BB}/Λ^4, $C_{\tilde{B}W}/\Lambda^4$, C_{BW}/Λ^4 and C_{WW}/Λ^4 is plotted in Figure 4.22 related to the FCC-hh collider. As before, the intersection points between the blue and orange lines give the limits of the couplings at 95% C.L. Hence, we obtain the 95% C.L limits for the different effective coupling C_{BB}/Λ^4, $C_{\tilde{B}W}/\Lambda^4$, C_{BW}/Λ^4 and C_{WW}/Λ^4 as [-0.597; 0.597], [-0.4803;0.4910], [-1.148; 1.148] and [-0.881; 0.881] respectively. In table 5.4, the obtained limits are summarized.

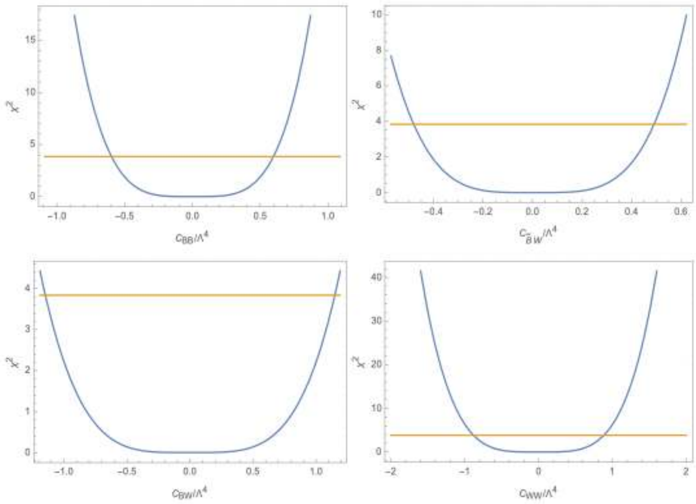

Figure 4.22. χ^2 (Blue solid line) as a function of the different effective couplings C_{BB}/Λ^4, $C_{\tilde{B}W}/\Lambda^4$, C_{BW}/Λ^4 and C_{WW}/Λ^4 for the process $pp \longrightarrow ZZ \longrightarrow \ell\ell\ell\ell$ at FCC-hh while the orange line represents χ^2= 3.84.

In Figure 4.23 we show the plot of the $\chi 2$ (represented by the blue solid line) versus the effective coupling C_{BB}/Λ^4, $C_{\tilde{B}W}/\Lambda^4$, C_{BW}/Λ^4 and C_{WW}/Λ^4 for the process $pp \longrightarrow ZZ \longrightarrow \ell\ell qq$ at FCC-hh future collider. In the same figure, the orange solid line represents the value of $\chi 2$ =3.84. The intersection points between the blue and the orange lines yield the 95% C.L limits for the coupling. Therefore, we find that the limits for the effective couplings C_{BB}/Λ^4, $C_{\tilde{B}W}/\Lambda^4$, C_{BW}/Λ^4 and C_{WW}/Λ^4 are [-0.29;0.29], [-0.22;0.23], [-0.53;0.53] and [-0.41;0.41] respectively. These ranges of the estimated limits are listed in table 5.3.

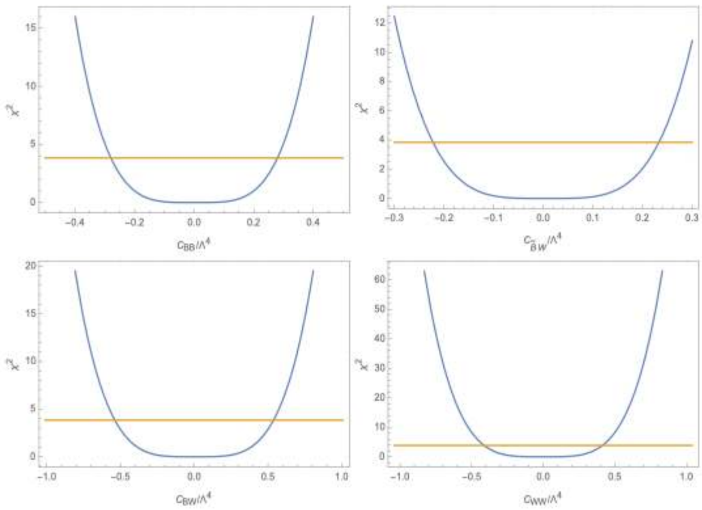

Figure 4.23. χ^2 (Blue solid line) as a function of the different effective couplings C_{BB}/Λ^4, $C_{\tilde{B}W}/\Lambda^4$, C_{BW}/Λ^4 and C_{WW}/Λ^4 for the process $pp \longrightarrow ZZ \longrightarrow \ell\ell qq$ at FCC-hh that has center of mass energy100TeV and luminosity 30ab^{-1}. In each plot the orange line represents χ^2 = 3.84 for one parameter.

In Figure 4.24 we display the plots of the χ^2 (blue solid line) versus the effective couplings C_{BB}/Λ^4 , $C_{\tilde{B}W}/\Lambda^4$, C_{BW}/Λ^4 and C_{WW}/Λ^4 . These plots correspond to the process $Z \longrightarrow qq\nu\nu$ at FCC-hh collider with center of mass energy100TeV and integrated luminosity 30 ab^{-1}. In each plot in the figure, the orange solid line represents the value χ^2 =3.84. As stated above, the values of the couplings at 95% C.L can be evaluated from the intersection points between the blue and orange lines in the corresponding plot. Thus, we infer from the figure that, the 95% C.L limits for the different effective coupling C_{BB}/Λ^4, $C_{\tilde{B}W}/\Lambda^4$, C_{BW}/Λ^4 and C_{WW}/Λ^4 are given as [-0.17;0.17], [-0.14;0.15], [-0.34;0.34] and [-0.26;0.26] respectively. The obtained limits will be presented in table 5.2 in the next chapter.

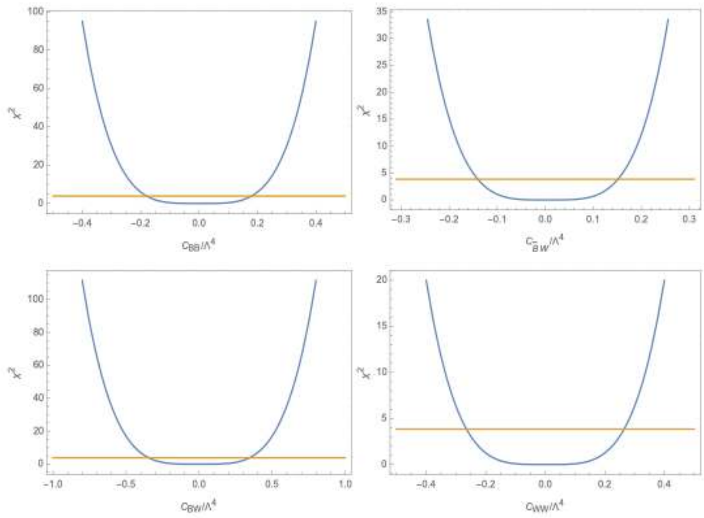

Figure 4.24. χ^2 (Blue solid line) as a function of the different effective couplings C_{BB}/Λ^4, $C_{\tilde{B}W}/\Lambda^4$, C_{BW}/Λ^4 and C_{WW}/Λ^4 for the process $pp \longrightarrow ZZ \longrightarrow qq\nu\nu$ at FCC-hh that has center of mass energy100TeV and luminosity 30 ab^{-1} where the orange line represents χ^2 =3.84 for one parameter.

In the analysis above, we considered the processes $pp \longrightarrow ZZ \longrightarrow \ell\ell\nu\nu$, $pp \longrightarrow ZZ \longrightarrow \ell\ell\ell\ell$, $pp \longrightarrow ZZ \longrightarrow \ell\ell qq$ and $pp \longrightarrow ZZ \longrightarrow qq\nu\nu$ at the FCC-hh collider with center of mass energy100TeV and integrated luminosity 30 ab^{-1}. In the following, we will perform similar analysis for the same processes but for different collider, namely the HE-LHC with c.m.e 27TeV and L_{int} 15ab^{-1}.

In Figure 4.25 we display the variation of the χ^2 (in green solid line) with the effective couplings C_{BB}/Λ^4, $C_{\tilde{B}W}/\Lambda^4$, C_{BW}/Λ^4 and C_{WW}/Λ^4 related to the process $pp \longrightarrow ZZ \longrightarrow \ell\ell\nu\nu$ for the HE-LHC collider with center of mass energy 27TeV and integrated luminosity 15ab^{-1}. In the plots, the orange line represents the value χ^2 =3.84. Again, the values of the couplings at 95% C.L. are determined from the intersection points between the green and orange lines. Consequently, we get the 95% C.L limits for the considered effective coupling C_{BB}/Λ^4, $C_{\tilde{B}W}/\Lambda^4$, C_{BW}/Λ^4 and C_{WW}/Λ^4 as [-5.12;5.12], [-3.94;3.99], [-8.75;8.75] and [-7.20;7.20] respectively. These allowed ranges for the couplings are listed in table 5.1.

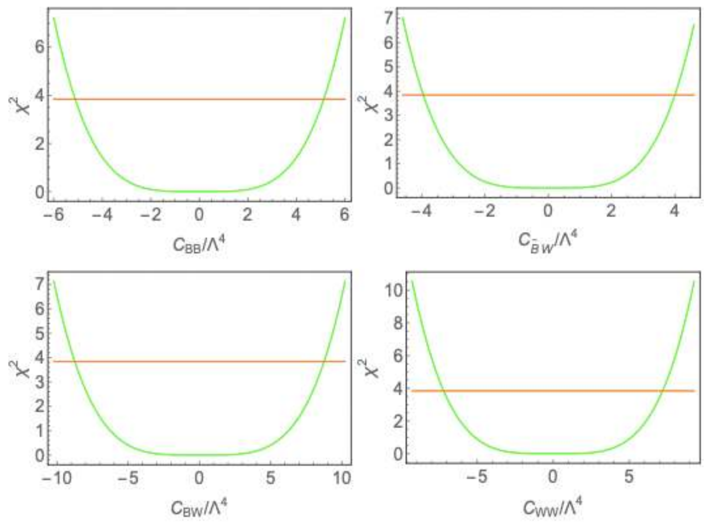

Figure 4.25. χ^2 (Green solid line) variation with the effective couplings C_{BB}/Λ^4, $C_{\tilde{B}W}/\Lambda^4$, C_{BW}/Λ^4 and C_{WW}/Λ^4 related to the process $pp \longrightarrow ZZ \longrightarrow \ell\ell\nu\nu$ for HE-LHC that has center of mass energy 27TeV and luminosity 15ab^{-1} where the orange line represents χ^2 =3.84 for one parameter.

Considering the process $pp \longrightarrow ZZ \longrightarrow \ell\ell\ell\ell$ for the same collider HE-LHC and same c.m.e and L_{int}, we plot χ^2 in green solid line as a function of the effective couplings C_{BB}/Λ^4, $C_{\tilde{B}W}/\Lambda^4$, C_{BW}/Λ^4 and C_{WW}/Λ^4 in Figure 4.26. The orange solid line in the figure represents the value χ^2 =3.84. To obtain the 95% C.L limits for the different effective couplings one needs to determine the intersection points between the green and orange lines. Clearly from the figure that, the limits for the coupling C_{BB}/Λ^4, $C_{\tilde{B}W}/\Lambda^4$, C_{BW}/Λ^4 and C_{WW}/Λ^4 read [-8.0016; 8.0016], [-6.179;6.229], [-13.673; 13.673] and [-11.245; 11.245], respectively. A summary of these limits will be given in table 5.4.

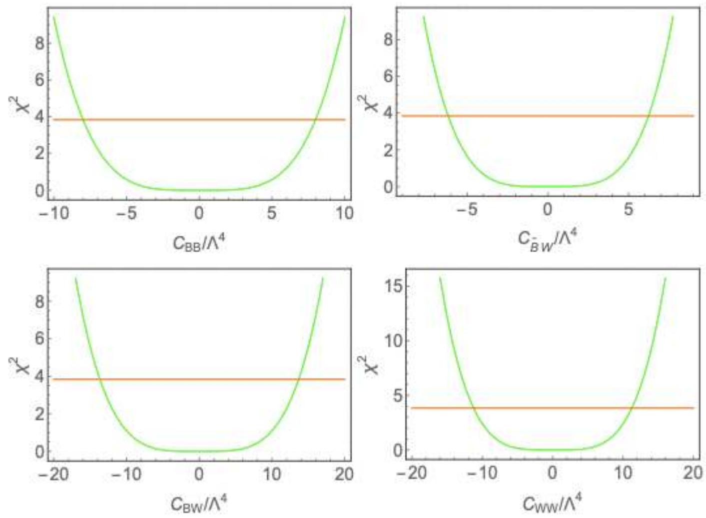

Figure 4.26. χ^2 (Green solid line) as a function of the different effective couplings C_{BB}/Λ^4, $C_{\tilde{B}W}/\Lambda^4$, C_{BW}/Λ^4 and C_{WW}/Λ^4 for the process $pp \longrightarrow ZZ \longrightarrow \ell\ell\ell\ell$ for HE-LHC that has center of mass energy 27TeV and luminosity 15ab^{-1} and the orange line is for χ^2 =3.84 for one parameter.

In Figure 4.27 each plot displays χ^2 (green solid line) as a function of one of the effective couplings C_{BB}/Λ^4, $C_{\tilde{B}W}/\Lambda^4$, C_{BW}/Λ^4 and C_{WW}/Λ^4 for the process $pp \longrightarrow ZZ \longrightarrow \ell\ell qq$ at the HE-LHC collider with center of mass energy 27 TeV and integrated luminosity 15 ab^{-1}. The orange line in every plot represents χ^2 =3.84. The 95% C.L limits on each effective coupling can be deduced from the intersection points between the green and orange lines in the corresponding plot. Therefore, the limits read [-3.74;3.74], [-2.88;2.93], [-6.40;6.40] and [-5.26;5.26] for the different effective couplings C_{BB}/Λ^4, $C_{\tilde{B}W}/\Lambda^4$, C_{BW}/Λ^4 and C_{WW}/Λ^4 respectively. In table 5.3 we present these obtained limits.

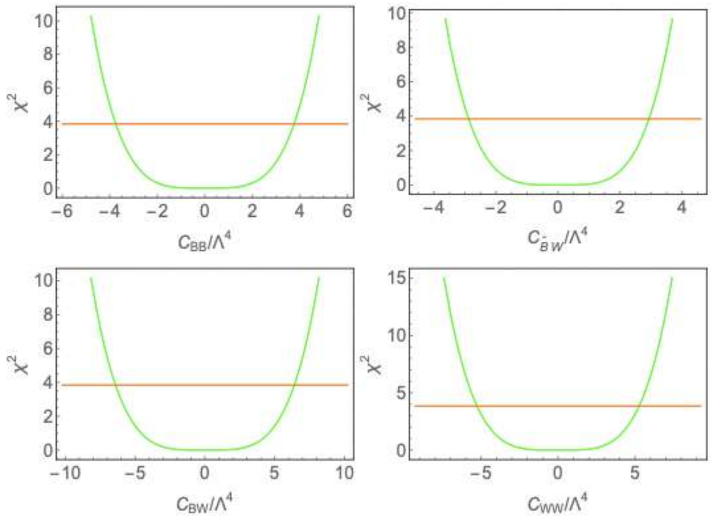

Figure 4.27. χ^2 (Green solid line) as a function of the effective couplings C_{BB}/Λ^4, $C_{\tilde{B}W}/\Lambda^4$, C_{BW}/Λ^4 and C_{WW}/Λ^4 related to the process $pp \longrightarrow ZZ \longrightarrow \ell\ell qq$ at HE-LHC that has center of mass energy 27 TeV and luminosity 15ab^{-1}. The orange line in each plot represents χ^2 =3.84 for one parameter.

In Figure 4.28, we plot χ^2 (in green solid line) versus each effective coupling C_{BB}/Λ^4, $C_{\tilde{B}W}/\Lambda^4$, C_{BW}/Λ^4 and C_{WW}/Λ^4 for the process $pp \longrightarrow ZZ \longrightarrow qq\nu\nu$ at the HE-LHC collider with c.m.e 27TeV and L_{int} 15ab^{-1}. As in the previous figures, the orange solid line represents the value χ^2 =3.84. The 95% C.L limits on the effective couplings C_{BB}/Λ^4, $C_{\tilde{B}W}/\Lambda^4$, C_{BW}/Λ^4 and C_{WW}/Λ^4 read [-2.40;2.40], [-1.83;1.88], [-4.10;4.10] and [-3.37;3.37] respectively. These limits follow from considering the intersection points between the green and orange lines and will be presented in table 5.2.

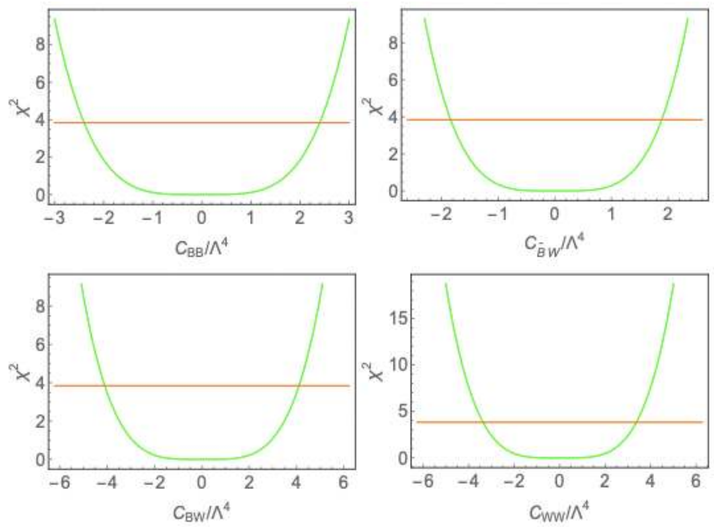

Figure 4.28. χ^2 (Green solid line) as a function of the effective couplings C_{BB}/Λ^4, $C_{\tilde{B}W}/\Lambda^4$, C_{BW}/Λ^4 and C_{WW}/Λ^4 for the process $pp \longrightarrow ZZ \longrightarrow qq\nu\nu$ for HE-LHC with center of mass energy 27 TeV and luminosity 15ab^{-1}. In the figure, the orange solid line represents χ^2 =3.84 for one parameter.

In Figure 4.29, Figuer 4.30, Figuer 4.31 and Figuer 4.32 below, we present our results for the processes $pp \longrightarrow ZZ \longrightarrow \ell\ell\nu\nu$, $pp \longrightarrow ZZ \longrightarrow \ell\ell\ell\ell$, $pp \longrightarrow ZZ \longrightarrow \ell\ell qq$ and $Z \longrightarrow qq\nu\nu$ at the HL-LHC collider with c.m.e 14TeV and L_{int} 3ab^{-1}. In all these figures the orange solid line represents χ2 =3.84 and the 95% C.L limit for the displayed effective coupling can be deduced from the intersection points between the red and orange lines.

In Figure 4.29, we plot the variation of the χ^2 (red solid line) with each effective coupling C_{BB}/Λ^4, $C_{\tilde{B}W}/\Lambda^4$, C_{BW}/Λ^4 and C_{WW}/Λ^4 for the process $pp \longrightarrow ZZ \longrightarrow \ell\ell\nu\nu$. The 95% C.L limits for the effective coupling C_{BB}/Λ^4, $C_{\tilde{B}W}/\Lambda^4$, C_{BW}/Λ^4 and C_{WW}/Λ^4 are [-20.5;20.5], [-50.33;50.61], [-34.7;34.7] and [-93.3;93.3] respectively and will be summarized in table 5.1.

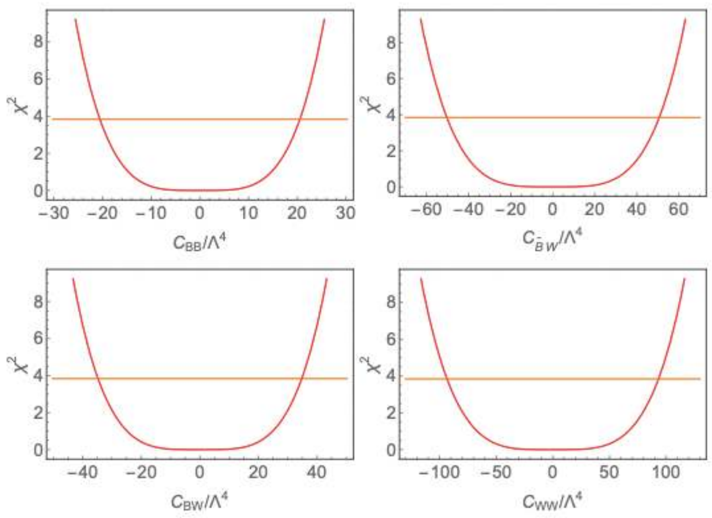

Figure 4.29. χ^2 (Red solid line) as a function of the different effective couplings C_{BB}/Λ^4, $C_{\tilde{B}W}/\Lambda^4$, C_{BW}/Λ^4 and C_{WW}/Λ^4 for the process $pp \longrightarrow ZZ \longrightarrow \ell\ell\nu\nu$ for HL-LHC that has center of mass energy14TeV and luminosity 3ab^{-1} where the orange line represents χ^2 =3.84 for one parameter.

In Figure 4.30, we plot χ^2 (red solid line) as a one variable function of the couplings C_{BB}/Λ^4, $C_{\tilde{B}W}/\Lambda^4$, C_{BW}/Λ^4 and C_{WW}/Λ^4 for the process $pp \longrightarrow ZZ \longrightarrow \ell\ell\ell\ell$. The 95% C.L limits, in this case, read [-32.07; 32.07], [-78.66; 78.94], [-54.29; 54.29] and [-142.73; 142.73] for the couplings C_{BB}/Λ^4, $C_{\tilde{B}W}/\Lambda^4$, C_{BW}/Λ^4 and C_{WW}/Λ^4 respectively. In table 5.4, we list these allowed ranges of the couplings.

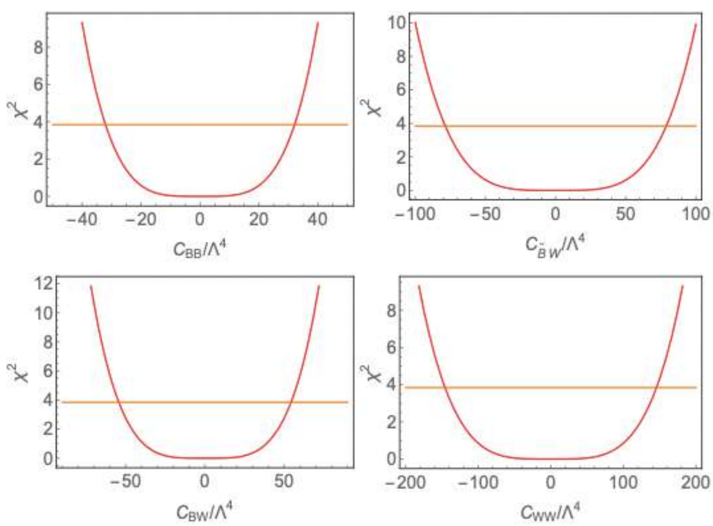

Figure 4.30. χ^2 (Red solid line) as a function of the couplings C_{BB}/Λ^4, $C_{\tilde{B}W}/\Lambda^4$, C_{BW}/Λ^4 and C_{WW}/Λ^4 for the process$pp \longrightarrow ZZ \longrightarrow \ell\ell\ell\ell$ at HL-LHC where the orange line represents χ^2 = 3.84 for one parameter.

In Figure 4.31, we show the variation of the χ^2 (red solid line) with the effective couplings C_{BB}/Λ^4, $C_{\tilde{B}W}/\Lambda^4$, C_{BW}/Λ^4 and C_{WW}/Λ^4 for the process $pp \longrightarrow ZZ \longrightarrow \ell\ell qq$. It shoud be noted that the solid orange line represents χ^2 =3.84. It is direct from the figure to derive the 95% C.L limits [-15.02;15.02], [-36.77;37.05], [-25.43;25.43] and [-68.26;68.26] on the effective couplings C_{BB}/Λ^4, $C_{\tilde{B}W}/\Lambda^4$, C_{BW}/Λ^4 and C_{WW}/Λ^4 are respectively. The obtained limits are given in table 5.3.

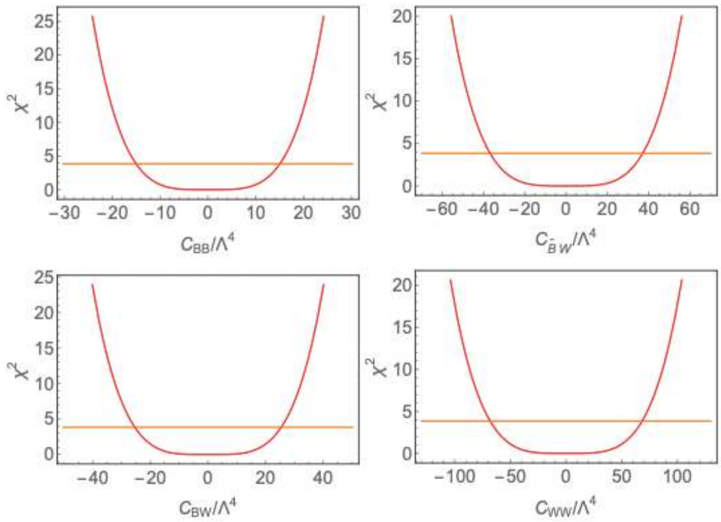

Figure 4.31. χ^2 (Red solid line) as a function of the different effective couplings C_{BB}/Λ^4, $C_{\tilde{B}W}/\Lambda^4$, C_{BW}/Λ^4 and C_{WW}/Λ^4 for the process $pp \longrightarrow ZZ \longrightarrow \ell\ell qq$. The orange line, in each plot, represents $\chi2$ =3.84 for one parameter.

In Fig4.32, we plot χ^2 (red solid line) as a function of the different effective couplings C_{BB}/Λ^4, $C_{\tilde{B}W}/\Lambda^4$, C_{BW}/Λ^4 and C_{WW}/Λ^4 related to the process $pp \longrightarrow ZZ \longrightarrow qq\nu\nu$ where the orange solid line represents $\chi2$ =3.84. From the figure, it is clear that, the 95% C.L limits for the effective couplings C_{BB}/Λ^4, $C_{\tilde{B}W}/\Lambda^4$, C_{BW}/Λ^4 and C_{WW}/Λ^4 read [-9.62;9.62], [-17.15;17.42], [-16.29;16.29] and [-43.72;43.72] respectively. The obtained limits will be summarized in table 5.2.

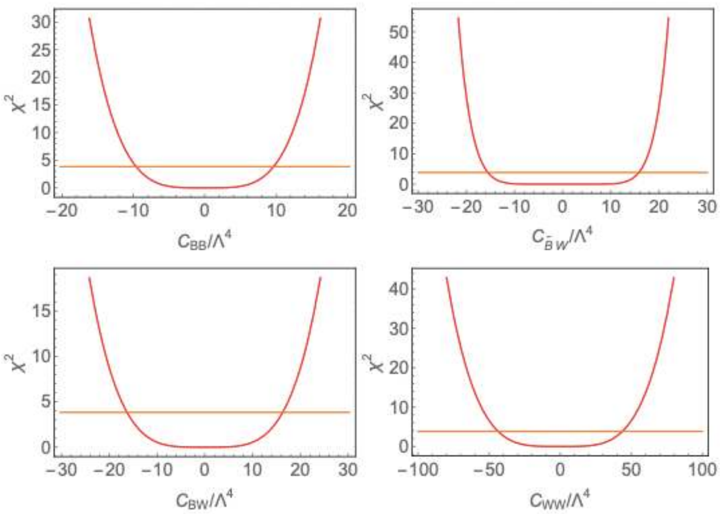

Figure 4.32. χ^2 (Red solid line) as a function of the different effective couplings C_{BB}/Λ^4, $C_{\tilde{B}W}/\Lambda^4$, C_{BW}/Λ^4 and C_{WW}/Λ^4 for the process $pp \longrightarrow ZZ \longrightarrow qq\nu\nu$.

In Fig4.33, Fig4.34, Fig4.35 and Fig4.36 below we discuss the processes $pp \longrightarrow ZZ \longrightarrow \ell\ell\nu\nu$,$pp \longrightarrow ZZ \longrightarrow \ell\ell\ell\ell$, $pp \longrightarrow ZZ \longrightarrow \ell\ell qq$ and $pp \longrightarrow ZZ \longrightarrow qq\nu\nu$ at LE-FCC collider with center of mass energy 37.5TeV and integrated luminosity 15ab^{-1}. In all these figures, the orange solid line represents χ^2 = 3.84. Similarly, to the previous cases, the 95% C.L limit for the studied effective coupling, in each plot, can be deduced from the intersection points between the black and the orange line.

In Figure 4.33, we show the χ^2 distribution (Black solid line) as a function of the effective couplings C_{BB}/Λ^4, $C_{\tilde{B}W}/\Lambda^4$, C_{BW}/Λ^4 and C_{WW}/Λ^4 for the process $pp \longrightarrow ZZ \longrightarrow \ell\ell\nu\nu$. We can deduce from the figure that the 95% C.L limits for the couplings C_{BB}/Λ^4, $C_{\tilde{B}W}/\Lambda^4$, C_{BW}/Λ^4 and C_{WW}/Λ^4 are [-2.79;2.79], [-2.11;2.13], [-5.63;5.63] and [-4.47;4.47] respectively. These allowed ranges of the limits will be listed in table 5.1.

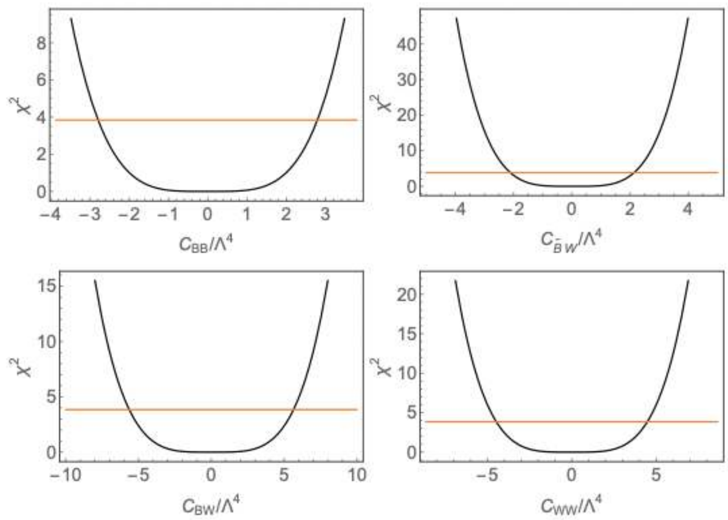

Figure 4.33. χ^2 (Black solid line) as a function of the different effective coupling C_{BB}/Λ^4, $C_{\tilde{B}W}/\Lambda^4$, C_{BW}/Λ^4 and C_{WW}/Λ^4 for the process $pp \longrightarrow ZZ \longrightarrow \ell\ell\nu\nu$.

In Figure 4.34, we show the variation of the χ^2 (Black solid line) with the effective couplings C_{BB}/Λ^4, $C_{\tilde{B}W}/\Lambda^4$, C_{BW}/Λ^4 and C_{WW}/Λ^4 for the process $pp \longrightarrow ZZ \longrightarrow \ell\ell\ell\ell$. One can deduce from the plots the 95% C.L limits [-4.3603; 4.3603], [-3.3048;3.3301], [-8.825; 8.825] and [-6.980; 6.980] corresponding to the effective couplings C_{BB}/Λ^4, $C_{\tilde{B}W}/\Lambda^4$, C_{BW}/Λ^4 and C_{WW}/Λ^4 respectively. These resulted limits will be displayed in table 5.4.

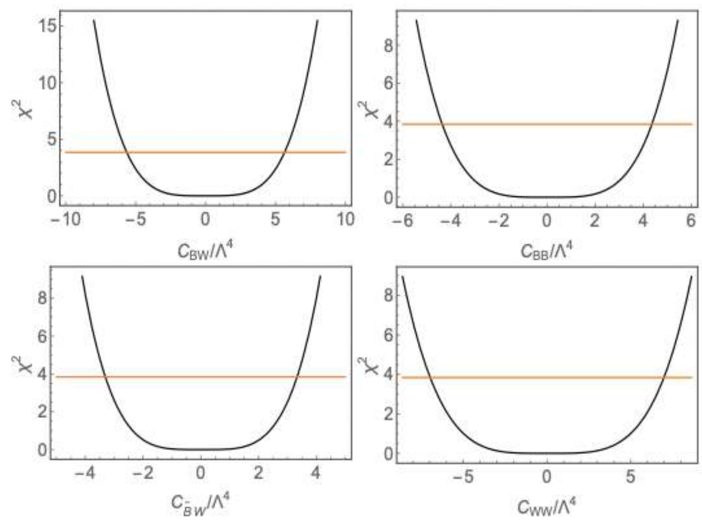

Figure 4.34. χ^2 (Black solid line) as a function of the different effective couplings C_{BB}/Λ^4, $C_{\tilde{B}W}/\Lambda^4$, C_{BW}/Λ^4 and C_{WW}/Λ^4 for the process $pp \longrightarrow ZZ \longrightarrow \ell\ell\ell\ell$.

In Figure 4.35, we show the plots of the χ^2 in black solid line as a function of the coupling s C_{BB}/Λ^4 , $C_{\tilde{B}W}/\Lambda^4$, C_{BW}/Λ^4 and C_{WW}/Λ^4 for the process $pp \longrightarrow ZZ \longrightarrow \ell\ell qq$. This results in the 95% C.L limits for the couplings C_{BB}/Λ^4 , $C_{\tilde{B}W}/\Lambda^4$, C_{BW}/Λ^4 and C_{WW}/Λ^4 as [-2.04;2.04], [-1.54;1.56], [-4.12;4.12]and [-3.27;3.27] respectively. The obtained results related to these limits are given in table 5.3.

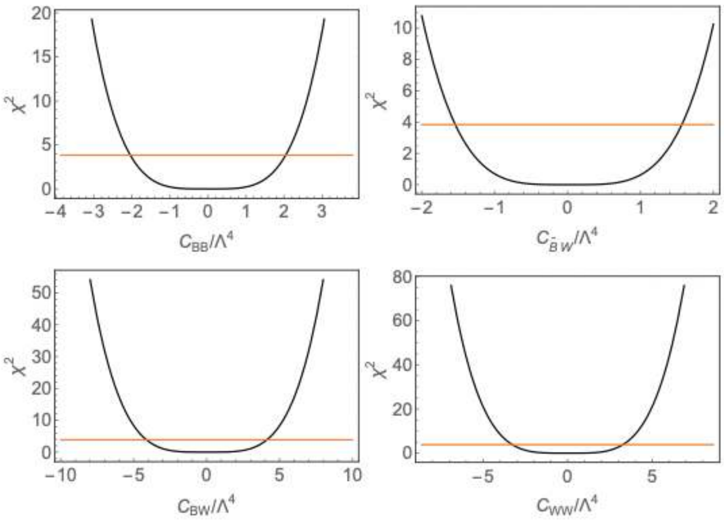

Figure 4.35. χ^2 (Black solid line) as a function of the different effective couplings C_{BB}/Λ^4, $C_{\tilde{B}W}/\Lambda^4$, C_{BW}/Λ^4 and C_{WW}/Λ^4 for the process $pp \longrightarrow ZZ \longrightarrow \ell\ell qq$.

Finally, for the process $pp \longrightarrow ZZ \longrightarrow qq\nu\nu$, the plots of χ^2 (given in black solid line) as a function of the couplings C_{BB}/Λ^4, $C_{\tilde{B}W}/\Lambda^4$, C_{BW}/Λ^4 and C_{WW}/Λ^4 are listed in Figure 4.36. The resultant 95% C.L limits for the couplings C_{BB}/Λ^4, $C_{\tilde{B}W}/\Lambda^4$, C_{BW}/Λ^4 and C_{WW}/Λ^4 read [-1.30;1.30], [-0.982;1.008[-2.64;2.64] and [-2.09;2.09] respectively. These allowed limits will be listed in table 5.2.

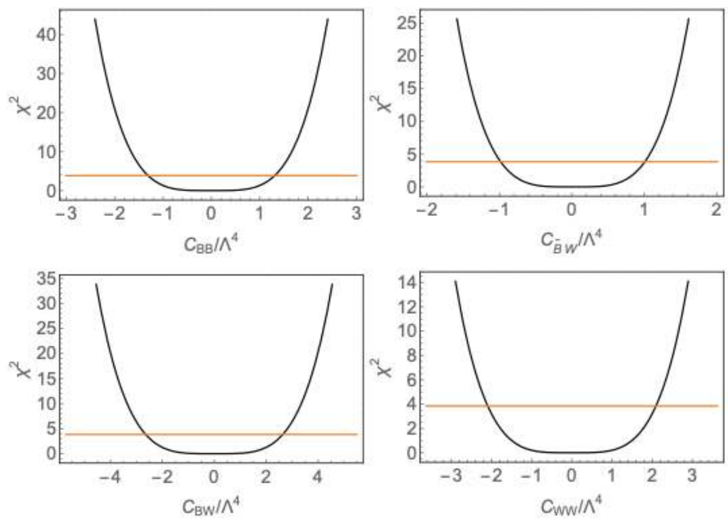

Figure 4.36. χ^2 (Black solid line) as a function of the different effective couplings C_{BB}/Λ^4, $C_{\tilde{B}W}/\Lambda^4$, C_{BW}/Λ^4 and C_{WW}/Λ^4 for the process $pp \longrightarrow ZZ \longrightarrow qq\nu\nu$.

5. CONCLUSIONS

Studying boson pair production in proton-proton future hadron colliders can be of great significance for search of new physics beyond SM. In particular, the production of two Z bosons is promising process in the search for neutral triple gauge boson couplings as it is forbidden in the SM at tree-level. This allows for new physics exploration of this pair production particularly for new physics models generating this process at tree-level. Moreover, investigation of this process can help to set constraints on the effective couplings contributing to this process as done in this thesis.

In this thesis, we have investigated the sensitivity of the anomalous triple gauge couplings via $pp \longrightarrow ZZ$ production in different decay channels of Z boson for various future circular hadron colliders (HL-LHC, HE-LHC, LE-FCC, and FCC) with effective field theory. Particularly, we considered the specific processes $pp \longrightarrow ZZ \longrightarrow \ell\ell\nu\nu$, $pp \longrightarrow ZZ \longrightarrow qq\nu\nu$, $pp \longrightarrow ZZ \longrightarrow \ell\ell qq$ as well as the process $pp \longrightarrow ZZ \longrightarrow \ell\ell\ell\ell$.

We have shown the distributions of the kinematic variables of the final state particles in each process and collider. Moreover, we have calculated the sensitivity of the anomalous triple gauge couplings in the effective field theory approach for the mentioned processes and colliders. Using the calculated sensitivities, we obtained the 95% C.L limits for the different effective couplings C_{BB}/Λ^4, $C_{\tilde{B}W}/\Lambda^4$, C_{BW}/Λ^4 and C_{WW}/Λ^4. Our results are summarized in Tables 5.1, 5.2, 5.3 and 5.4 below.

In Table 5.1, we list our results regarding the limits for the effective couplings contributing to the process $pp \longrightarrow ZZ \longrightarrow \ell\ell\nu\nu$ for different future colliders. Our obtained result for the $C_{\tilde{B}W}/\Lambda^4$ coupling is of the same order of magnitude for HE-LHC and LE-FCC colliders and one order of magnitude smaller than current ATLAS (79) result [-4.0 TeV^{-4} - 4.0 TeV^{-4}] via $pp \longrightarrow ZZ \longrightarrow \ell\ell\nu\nu$ process. It should be noted that the ATLAS limit is corresponding to the LHC run at center of mass energy 13 TeV and integrated luminosity 36.1 fb^{-1}. For the HL-LHC collider with center of mass energy 14 TeV and integrated luminosity 3ab^{-1}, our obtained limits for the couplings are much bigger than the corresponding ones of the other colliders as can be seen from the table. Another remark, from the table, the range of the allowed effective couplings in case of the FCC-hh collider is small compared to the allowed ones in the other colliders. This can be attributed to the fact that the FCC-hh collider has the highest center of mass energy among all other colliders.

Table 5.1. The obtained limits on the effective couplings related to the process $pp \longrightarrow ZZ \longrightarrow \ell\ell\nu\nu$ for different future colliders.

	$C_{BB}/\Lambda^4(TeV^{-4})$	$C_{\tilde{B}W}/\Lambda^4(TeV^{-4})$	$C_{BW}/\Lambda^4(TeV^{-4})$	$C_{WW}/\Lambda^4(TeV^{-4})$
HL-LHC	[-20.5;20.5]	[-50.33;50.61]	[-34.7;34.7]	[-93.3;93.3]
HE-LHC	[-5.12;5.12]	[-3.94;3.99]	[-8.75;8.75]	[-7.20;7.20]
LE-FCC	[-2.79;2.79]	[-2.11;2.13]	[-5.63;5.63]	[-4.47;4.47]
FCC-hh	[-0.38;0.38]	[-0.30;0.31]	[-0.73;0.73]	[-0.56;0.56]

We turn now to Table 5.2 in which we present our results for the 95% C.L. limits for the effective couplings of the process $pp \longrightarrow ZZ \longrightarrow qq\nu\nu$. There is no reported result by ATLAS and CMS collaboration at LHC collider related to this process. We see from the last row in Table 5.2 that, the allowed range of the effective couplings for the case of the FCC-hh collider is one order of magnitude smaller than the allowed ones in the HE-LHC and LE-FCC colliders. Moreover, it is two orders of magnitudes smaller than the allowed range in the HL-LHC collider. As explained above, this is due to the fact that the FCC-hh collider has the highest center of mass energy compared to the others. In fact, as one can see from the table, the FCC-hh collider gives the best limits on all effective couplings.

Table 5.2. The obtained limits on the effective couplings related to the results of the process $pp \longrightarrow ZZ \longrightarrow qq\nu\nu$ for different future colliders.

	$C_{BB}/\Lambda^4(TeV^{-4})$	$C_{\tilde{B}W}/\Lambda^4(TeV^{-4})$	$C_{BW}/\Lambda^4(TeV^{-4})$	$C_{WW}/\Lambda^4(TeV^{-4})$
HL-LHC	[-9.62;9.62]	[-17.15;17.42]	[-16.29;16.29]	[-43.72;43.72]
HE-LHC	[-2.40;2.40]	[-1.83;1.88]	[-4.10;4.10]	[-3.37;3.37]
LE-FCC	[-1.30;1.30]	[-0.982;1.008]	[-2.64;2.64]	[-2.09;2.09]
FCC-hh	[-0.17;0.17]	[-0.14;0.15]	[-0.34;0.34]	[-0.26;0.26]

Regarding table 5.3, we display our derived limits for the effective couplings of the process $pp \longrightarrow ZZ \longrightarrow \ell\ell qq$ for the same set of the future colliders. There are no limits obtained by ATLAS and CMS collaborators for this process. Again, the same conclusions regarding the limits presented in table 5.2 holds also here for this table.

Table 5.3. Estimated limits on the effective couplings related to the results of the process $pp \longrightarrow ZZ \longrightarrow \ell\ell qq$ for different future colliders.

	$C_{BB}/\Lambda^4(TeV^{-4})$	$C_{\tilde{B}W}/\Lambda^4(TeV^{-4})$	$C_{BW}/\Lambda^4(TeV^{-4})$	$C_{WW}/\Lambda^4(TeV^{-4})$
HL-LHC	[-15.02;15.02]	[-36.77;37.05]	[-25.43;25.43]	[-68.26;68.26]
HE-LHC	[-3.74;3.74]	[-2.88;2.93]	[-6.40;6.40]	[-5.26;5.26]
LE-FCC	[-2.04;2.04]	[-1.54;1.56]	[-4.12;4.12]	[-3.27;3.27]
FCC-hh	[-0.29;0.29]	[-0.22;0.23]	[-0.53;0.53]	[-0.41;0.41]

The current 95% C.L limits for the effective couplings $C_{BB}/\Lambda^4(TeV^{-4})$, $C_{\tilde{B}W}/\Lambda^4(TeV^{-4})$, $C_{BW}/\Lambda^4(TeV^{-4})$ and $C_{WW}/\Lambda^4(TeV^{-4})$ from ATLAS (80) experiment via $pp \longrightarrow ZZ \longrightarrow \ell\ell\ell\ell$ process are [-2.7; 2.8], [-5.9; 5.9], [-3.3; 3.3] and [-3.0; 3.0], respectively. These limits based on the data obtained from the LHC run at center of mass energy 13 TeV and integrated luminosity 36.1 fb^{-1}. On the other hand, the limits for the same set of the effective couplings in the same order as listed above from the CMS collaboration for the same process are reported as (81) [-1.2; 1.2], [-2.3; 2.5], [-1.4; 1.3] and [-1.4; 1.2], respectively. The limits were derived from the data obtained from the LHC run at center of mass energy 13 TeV and integrated luminosity 137 fb^{-1}. From these results, both ATLAS and CMS obtained limits of the same order of magnitude for the corresponding effective couplings. In order to compare our derived limits with the corresponding ones from ATLAS and CMS collaborations via $pp \longrightarrow ZZ \longrightarrow \ell\ell\ell\ell$ process, we list in Table 5.4 our results for different colliders. Our limits for the HL-LHC and HE-LHC colliders look bigger for the corresponding couplings. As can be seen from the table, the FCC-hh collider gives the best limits for all effective couplings. Additionally, regarding FCC-hh collider, our result for the limit on the effective coupling $C_{BW}/\Lambda^4(TeV^{-4})$ is of the same order of magnitude as the limits from ATLAS and CMS collaborations. Besides, for the same collider, our result for the limits for the effective coupling $C_{\tilde{B}W}/\Lambda^4(TeV^{-4})$ is one order of magnitude smaller than those one obtained by CMS and ATLAS collaborations while for the last two couplings the CMS and ATLAS are larger by only factor 2.

Table 5.4. Dervied limits on the effective couplings related to the results of the process $pp \longrightarrow ZZ \longrightarrow \ell\ell\ell\ell$ for different future colliders.

	$C_{BB}/\Lambda^4(TeV^{-4})$	$C_{\tilde{B}W}/\Lambda^4(TeV^{-4})$	$C_{BW}/\Lambda^4(TeV^{-4})$	$C_{WW}/\Lambda^4(TeV^{-4})$
HL-LHC	[-32.07; 32.07]	[-78.66; 78.94]	[-54.29; 54.29]	[-142.73; 142.73]
HE-LHC	[-8.0016; 8.0016]	[-6.179;6.229]	[-13.673; 13.673]	[-11.245; 11.245]
LE-FCC	[-4.3603; 4.3603]	[-3.3048;3.3301]	[-8.825; 8.825]	[-6.980; 6.980]
FCC-hh	[-0.597; 0.597]	[-0.4803;0.4910]	[-1.148; 1.148]	[-0.881; 0.881]

We end our conclusion by stressing on the important outcomes of our thesis which we summarize in the following. Regarding the HL-LHC collider, the obtained limits for all effective couplings are loose. The FCC-hh collider gives the best 95% C.L limits for all effective couplings compared to the set of future colliders considered in this thesis. These limits are of the same orders of their corresponding ones obtained by ATLAS and CMS collaborations. However, our derived limits for all effective couplings are stronger than those reported by ATLAS and CMS collaborations. Finally, $pp \longrightarrow ZZ \longrightarrow qq\nu\nu$ gives the best 95% C.L limits for all couplings studied in this thesis at each collider among the different final state processes.

6. REFERENCES

"Vancouver citation system was used in this thesis."

(1–81)

1. Neubauer MS. Diboson Production at Colliders. Annual Review of Nuclear and Particle Science. 2011 Nov 23;61(1):223–50.

2. Hsu SC. Measurement of the ZZ production cross section and limits on anomalous neutral triple gauge couplings in proton-proton collisions at sqrt{s} =7 TeV with the ATLAS detector. 2011 Sep 29;

3. Azatov A, Barducci D, Venturini E. Precision diboson measurements at hadron colliders. 2019 Jan 15;

4. Backer M. Measurement of ZZ production and search for anomalous neutral triple gauge couplings in pp collisions at √s =13 TeV with the ATLAS experiment. 2022 Aug 26;

5. Fermi E. Versuch einer Theorie der? - Strahlen. I. Zeitschrift f□r Physik. 1934 Mar;88(3–4):161–77.

6. Fritzsch H, Gell-Mann M, Leutwyler H. Advantages of the color octet gluon picture. Physics Letters B. 1973 Nov;47(4):365–8.

7. Weinberg S. A Model of Leptons. Phys Rev Lett. 1967 Nov 20;19(21):1264–6.

8. Glashow SL. Partial-symmetries of weak interactions. Nuclear Physics. 1961 Feb;22(4):579–88.

9. N. Svartholm (Almqvist and Wiksell). Elementary Particle Theory. Stokholm. 1969;367.

10. File: Standard Model of Elementary Particles Anti.svg - Wikimedia Commons [Internet]. [cited 2022 Jun 7]. Available from: https://commons.wikimedia.org/wiki/File:Standard_Model_of_Elementary_Particles_Anti.svg.

11. F. Halzen and A. Martin, Quarks and leptons: an introductory course in modern particle physics, Wiley, 1984.

12. Englert F, Brout R. Broken symmetry and the mass of gauge vector mesons. Physical Review Letters [Internet]. 1964 Aug 31 [cited 2022 May 1];13(9):321–3. Available from: https://journals.aps.org/prl/abstract/10.1103/PhysRevLett.13.321.

13. Higgs PW. Broken symmetries and the masses of gauge bosons. Physical Review Letters [Internet]. 1964 Oct 19 [cited 2022 May 1];13(16):508–9. Available from: https://journals.aps.org/prl/abstract/10.1103/PhysRevLett.13.508.

14. Guralnik G et al. Global Conservation Laws and Massless Particles, Phys. Rev. Lett. 13, 585-587(1964).

15. Hagiwara K, Hikasa K, Nakamura K, Tanabashi M, Aguilar-Benitez M, Amsler C, et al. Review of Particle Properties. Physical Review D. 2002 Jul 1;66(1):010001.

16. Dris Boubaa (Algiers, Ecole Normale Superieure and Hassiba Benbouali U., Chlef), Gaber Faisel (Suleyman Demirel U.), Shaaban Khalil (Zewail City Sci. Technol., Giza) e-Print: 2005.08069 [hep-ph].

17. Zwicky F, Die Rotverschiebung von extragalaktischen Nebeln, Helv. Phys. Acta 6, 110-127(1933).

18. Sakharov AD. Violation of *CP* in variance, *C* asymmetry, and baryon asymmetry of the universe. Soviet Physics Uspekhi. 1991 May 31;34(5):392–3.

19. Nardi E., Z', new fermions, and flavor changing process. Constraints on E(6) models from $\mu \rightarrow eee$ Physical Review D. 1993 Aug 1;48(3):1240–7.

20. L. F. Abbott, P. Sikivie and M. B. Wise, Constraints on charged-Higgs-boson couplings, Phys. Rev. D 21, 1393 (1980).

21. Ma E. Verifiable radiative seesaw mechanism of neutrino mass and dark matter. Physical Review D. 2006 Apr 14;73(7):077301.

22. Masip M, Pomarol A. Effects of standard model Kaluza-Klein excitations on electroweak observables. Physical Review D. 1999 Oct 8;60(9):096005.

23. [H. P. Nilles, "Supersymmetry, Supergravity and Particle Physics," Phys. Rept. 110 (1984), 1-162.

24. Kane GL, editor. Perspectives On Supersymmetry. Vol. 18. World Scientific Publishing Co. Pte. Ltd.; 1998.

25. K. Hagiwara, R.D. Peccei, D. Zeppenfeld, K. Hikasa, Probing the weak boson sector in e+e− → W+W−, Nucl. Phys. B 282 (1987) 253–307. .

26. G.J. Gounaris, J. Layssac, F.M. Renard, Signatures of the anomalous Zγ and ZZ production at the lepton and hadron colliders, Phys. Rev. D 61 (2000) 073013, arXiv:hep-ph/9910395 [hep-ph].

27. U. Baur, D.L. Rainwater, Probing neutral gauge boson selfinteractions in ZZ production at hadron colliders, Phys. Rev. D 62 (2000) 113011, arXiv:hep-ph/0008063 [hep-ph].

28. R. Rahaman, R.K. Singh, On the choice of beam polarization in e+e− → ZZ/Zγ and anomalous triple gaugeboson couplings, Eur. Phys. J. C 77 (8) (2017) 521, arXiv:1703.06437 [hep-ph].

29. Baur U, Rainwater D. Probing neutral gauge boson self-interactions in ZZ production at hadron colliders. Physical Review D. 2000 Nov;62(11):113011.

30. Green DR, Meade P, Pleier MA. Multiboson interactions at the LHC. Rev Mod Phys. 2017 Sep 20;89(3):035008.

31. C. Degrande et al., E_ective _eld theory: a modern approach to anomalous couplings, Annals Phys. 335 (2013) p. 21, arXiv: 1205.4231 [hep-ph].

32. Celine Degrande, Nicolas Greiner, Wolfgang Kilian, Olivier Mattelaer, Harrison Mebane, et al. Effective Field Theory: A Modern Approach to Anomalous Couplings. Annals Phys., 335:21–32, 2013.

33. C. Degrande, A basis of dimension-eight operators for anomalous neutral triple gauge boson interactions, JHEP 02 (2014) p. 101, arXiv: 1308.6323 [hep-ph].

34. M.~Aaboud \ M.~Becker, ``Measurement of ZZ production and search for anomalous neutral triple gauge couplings in pp collisions at \sqrt s = 13 TeV with the ATLAS

experiment,’’doi:10.25358/openscience-4467
(2019)doi:10.1007/JHEP10(2019)127[arXiv:1905.07163 [hep-ex]].

35. Yilmaz A. Search for the limits on anomalous neutral triple gauge couplings via ZZ production in the ℓℓνν channel at FCC-hh. Nucl Phys B. 2021 Aug;969:115471.

36. Brüning O, Collier P. Building a behemoth. Nature. 2007 Jul 18;448(7151):285–9.

37. Evans L, Bryant P. LHC Machine. Journal of Instrumentation. 2008 Aug 14;3(08):S08001–S08001.

38. P. Gessinger-Befurt and S. Tapprogge, Search for new heavy charged gauge bosons with the ATLAS detector, Presented 15 May 2017, MA thesis, 2017, url: https://cds.cern.ch/record/2276657.

39. G.~Aad \textit{et al.} [ATLAS],``Observation of a new particle in the search for the Standard Model Higgs boson with the ATLAS detector at the LHC,’’Phys. Lett. B \textbf{716}, 1-29 (2012) doi:10.1016/j.physletb.2012.08.020 [arXiv:1207.7214 [hep-ex]].

40. C. Quigg, Reviews of Accelerator Science and Technol- ogy 10, 3 (2019), arXiv preprint arXiv:1808.06036.

41. N. Arkani-Hamed, T. Han, M. Mangano, and L.-T. Wang, Physics Reports 652, 1 (2016).

42. CEPC Study Group, (2018), arXiv:1809.00285 [physics.acc-ph]. arXiv:2003.09084v1.

43. M. Benedikt et al., Annual Review of Nuclear and Par- ticle Science 69 (2019). arXiv:2003.09084v1.

44. BURKHARD SCHMIDT, THE HIGH-LUMINOSITY UPGRADE OF THE LHC: PHYSICS AND TECHNOLOGY CHALLENGES FOR THE ACCELERATOR AND THE EXPERIMENTS, J. PHYS.: CONF. SER. 706 022002, 2016.

45. Agostini P, Aksakal H, Alekhin S, Allport PP, Andari N, Andre KDJ, et al. The Large Hadron–Electron Collider at the HL-LHC. Journal of Physics G: Nuclear and Particle Physics. 2021 Nov 1;48(11):110501.

46. X.~Cid Vidal, M.~D’Onofrio, P.~J.~Fox, R.~Torre, K.~A.~Ulmer, A.~Aboubrahim, A.~Albert, J.~Alimena, B.~C.~Allanach and C.~Alpigiani, \textit{et al.}``Report from Working Group 3: Beyond the Standard Model physics at the HL-LHC and HE-LHC,’’CERN Yellow Rep. Monogr. \textb f{7}, 585-865 (2019) doi:10.23731/CYRM-2019-007.585 [arXiv:1812.07831 [hep-ph]].

47. G. Apollinari, I. Béjar Alonso, O. Brüning, P. Fessia, M. Lamont, L. Rossi, and L. Tavian, High-Luminosity Large Hadron Collider (HL-LHC), CERN Yellow Report 004 (2017).

48. J.~Keintzel, M.~Crouch, M.~Hofer, T.~Risselada, R.~Tom\’as, F.~Zimmermann and L.~van Riesen-Haupt``HE-LHC optics design options,’’doi:10.18429/JACoW-IPAC2019-MOPMP026.

49. Abada A, Abbrescia M, AbdusSalam SS, Abdyukhanov I, Abelleira Fernandez J, Abramov A, et al. HE-LHC: The High-Energy Large Hadron Collider. Eur Phys J Spec Top. 2019 Jul 16;228(5):1109–382.

50. A. Abada, M. Abbrescia, S.S. Abdussalam, I. Abdyukhanov, J. Abelleira Fernandez, et al. HE-LHC: The High-Energy Large Hadron Collider: Future Circular Collider Conceptual Design Report Volume 4. Eur.Phys.J.ST, 2019, 228 (5), pp.1109-1382. ⟨10.1140/epjst/e2019-900088-6⟩. ⟨hal-02279031⟩.

51. Mangano, Michelangelo. Physics potential of a low-energy FCC-hh. No. CERN-FCC-PHYS-2019-0001. FCC-DRAFT-PHYS-2019-002, 2019.

52. Helsens C, Jamin D, Mangano ML, Rizzo TG, Selvaggi M. Heavy resonances at energy-frontier hadron colliders. The European Physical Journal C. 2019 Jul 8;79(7):569.

53. Abada A, Abbrescia M, AbdusSalam SS, Abdyukhanov I, Fernandez JA, Abramov A, et al. FCC Physics Opportunities. The European Physical Journal C. 2019 Jun 5;79(6):474.

54. Abada A, Abbrescia M, AbdusSalam SS, Abdyukhanov I, Abelleira Fernandez J, Abramov A, et al. FCC-hh: The Hadron Collider. Eur Phys J Spec Top. 2019 Jul 5;228(4):755–1107.

55. O.S. Br□uning, P. Collier, P. Lebrun, S. Myers, R. Ostojic, J. Poole, P. Proudlock, LHC Design Report, CERN Yellow Reports: Monographs (CERN, Geneva, Switzerland, 2004), http://cds.cern.ch/record/782076.

56. R. Contino et al., Physics at a 100 TeV pp collider: Higgs and EW symmetry breaking studies, CERN Yellow Report (2017) no. 3, 255–440, arXiv:1606.09408 [hep-ph].

57. Gonçalves D, Han T, Mukhopadhyay S. Off-Shell Higgs Probe of Naturalness. Phys Rev Lett. 2018 Mar 15;120(11):111801.

58. ATLAS Collaboration. Constraints on off-shell Higgs boson production and the Higgs boson total width in $ZZ\to4\ell$ and $ZZ\to2\ell2\nu$ final states with the ATLAS detector. 2018 Aug 3;

59. ATLAS Collaboration. Measurement of ZZ production in the $\ell\ell\nu\nu$ final state with the ATLAS detector in pp collisions at $\sqrt{s} = 13$ TeV. 2019 May 17;

60. Vasiliki Kouskoura, Study of diboson production (Z orW) in the ATLAS experiment from their leptonic decays Ph.D. thesis 2014.

61. R.L.~Workman et al. [Particle Data Group], ``Review of Particle Physics,'' to be published (2022).

62. T. Stelzer and W. F. Long, Automatic generation of tree level helicity amplitudes, Comput. Phys. Commun. 81 (1994) 357–371, [hep-ph/9401258].

63. F. Maltoni and T. Stelzer, MadEvent: Automatic event generation with MadGraph, JHEP 02 (2003) 027, [hep-ph/0208156].

64. J. Alwall et al., MadGraph/MadEvent v4: The New Web Generation, JHEP 09 (2007) 028, [0706.2334].

65. Alwall J, Frederix R, Frixione S, Hirschi V, Maltoni F, Mattelaer O, et al. The automated computation of tree-level and next-to-leading order differential cross sections, and their matching to parton shower simulations. Journal of High Energy Physics. 2014 Jul 17;2014(7):79.

66. Degrande C, Duhr C, Fuks B, Grellscheid D, Mattelaer O, and Reiter T (2012) "UFO - The Universal FeynRules Output", Comput. Phys. Commun., 183:1201–1214.

67. Buckley A, Ferrando J, Lloyd S, Nordström K, Page B, Rüfenacht M, et al. LHAPDF6: parton density access in the LHC precision era. The European Physical Journal C. 2015 Mar 20;75(3):132.

68. R. D. BALL, V. BERTONE, S. CARRAZZA, C. S. DEANS, L. D. DEBBIO, S. FORTE, A. GU_ANTI, N. P. HARTLAND, J. I. LATORRE, J. ROJO, AND M. UBIALI, PARTON DISTRIBUTIONS WITH LHC DATA, NUCLEAR PHYSICS B 867, 244 (2013).

69. J. de Favereau, C. Delaere, P. Demin, A. Giammanco, V. Lema^_tre, A. Mertens, and M. Selvaggi, a modular framework for fast simulation of a generic collider experiment, Journal of High Energy Physics 2014 (2014), 10.1007/jhep02(2014)057.

70. P. Demin, \https://cp3.irmp.ucl.ac.be/projects/exrootanalysis,".

71. R. Brun and F. Rademakers, Nuclear Instruments and Methods in Physics Research Section A: Accelerators, Spectrometers, Detectors and Associated Equipment 389, 81 (1997), new Computing Techniques in Physics Research V.

72. de Aquino P, Link W, Maltoni F, Mattelaer O, Stelzer T. ALOHA: Automatic libraries of helicity amplitudes for Feynman diagram computations. Comput Phys Commun. 2012 Oct;183(10):2254–63.

73. Sjöstrand T, Ask S, Christiansen JR, Corke R, Desai N, Ilten P, et al. An introduction to PYTHIA 8.2. Comput Phys Commun. 2015 Jun; 191:159–77.

74. H.~Murayama, I.~Watanabe and K.~Hagiwara, HELAS: HELicity amplitude subroutines for Feynman diagram evaluations, KEK-91-11.

75. Maltoni F, Stelzer T. MadEvent: automatic event generation with MadGraph. Journal of High Energy Physics. 2003 Feb 17;2003(02):027–027.

76. Christensen ND, Duhr C. FeynRules – Feynman rules made easy. Comput Phys Commun. 2009 Sep;180(9):1614–41.

77. Alloul A, Christensen ND, Degrande C, Duhr C, Fuks B. FeynRules 2.0 — A complete toolbox for tree-level phenomenology. Comput Phys Commun. 2014 Aug;185(8):2250–300.

78. A. M. Sirunyan, A. Tumasyan, W. Adam, F. Ambrogi, E. Asilar, T. Bergauer, J. Brandstetter, E. Brondolin.

79. Measurement of ZZ production in the llvv final state with the ATLAS detector in pp collisions at TeV ATLAS Collaboration • Morad Aaboud (Oujda U.) et al. e-Print: 1905.07163 [hep-ex] DOI: 10.1007/JHEP10(2019)127 (publication) Published in: JHEP 10 (2019), 127.

80. ATLAS Collaboration. $ZZ \to \ell^{+}\ell^{-}\ell^{\prime +}\ell^{\prime -}$ cross-section measurements and search for anomalous triple gauge couplings in 13 TeV pp collisions with the ATLAS detector. 2017 Sep 22;

81. Sirunyan AM, Tumasyan A, Adam W, Ambrogi F, Bergauer T, Dragicevic M, et al. Measurements of $${\mathrm{p}} {\mathrm{p}} \rightarrow {\mathrm{Z}} {\mathrm{Z}} $$ production cross sections and constraints on anomalous triple gauge couplings at $$\sqrt{s} = 13\,\text {TeV} $$. The European Physical Journal C. 2021 Mar 1;81(3):200.